




Lagrangian coherent structures control solute dispersion in heterogeneous poroelastic media

Junhong Wu  and Daniel Lester *

School of Engineering, RMIT University, Melbourne, Victoria 3000, Australia

Michael G. Trefry 

Independent Researcher, Perth, Western Australia 6000, Australia

Guy Metcalfe 

Swinburne University of Technology, Melbourne, Victoria 3000 Australia



(Received 22 November 2023; accepted 6 March 2024; published 9 April 2024)

Recent work has demonstrated that Lagrangian chaos can arise at the Darcy scale in even simple poroelastic media, relevant across geophysical, biophysical, and industrial domains. Key factors controlling the onset of chaotic advection in poroelastic media flow include medium heterogeneity, compressibility, and transient forcing. Here we focus on how the range of Lagrangian coherent structures (LCSs) present in poroelastic flows influences the transport of diffusive solutes. We use a minimal two-dimensional sinusoidally forced poroelastic computational model to show that LCS interactions impact the dispersion of solute plumes via the establishment of minimum flux manifolds, leading to strongly anomalous plume moments and solute residence time distributions. We interpret these results with fluid element stretching distributions and local Lyapunov exponents. Anomalous features persist even at low Péclet number. Our data show that solute dispersion in poroelastic systems subject to transient forcing can only be understood by resolving the LCSs of these complex flows.

DOI: [10.1103/PhysRevFluids.9.044501](https://doi.org/10.1103/PhysRevFluids.9.044501)

I. INTRODUCTION

Many saturated porous materials are “soft” or poroelastic in that the solid matrix can deform appreciably due to spatial and/or temporal variations in the local fluid pressure. These soft porous materials include biological tissues, geological media, concentrated suspensions, and advanced materials; they span applications from energy, water, and mineral resources to environmental management, human health, material processing, and biotechnology. In many applications, poroelastic materials are subject to transient forcings that arise from, e.g., seasonal, tidal, cardiovascular, or other external forcings, leading to complex fluidic transport phenomena that are currently not well understood. For example, fluidic transport in brain tissue, which is considered to be central to many diseases including Parkinson’s and Alzheimer’s, is thought to be driven by periodic forcing via surrounding blood vessels [1]. Similarly, the distribution and migration of contaminants in transiently forced poroelastic systems differs significantly from those subject to steady flow [2].

Fluidic transport in transiently forced poroelastic media is a rich and complex process [3], chiefly due to (i) bidirectional coupling of fluid flow and solid deformation [4,5], (ii) interactions

*daniel.lester@rmit.edu.au

between the forcing timescale and the relaxation timescale of the poroelastic medium [6], and (iii) heterogeneity of the medium properties. The fluidic transport process begins as fluids permeate through interconnected pores, driven by pressure gradients and permeability distributions as dictated by Darcy's law [7]. Simultaneously the poroelastic medium deforms in response to changes in pore pressure, resulting in local changes in porosity and permeability, altering fluid flow pathways and thus fluidic transport. Under an applied transient forcing pressure at a boundary, such as, for example, cardiovascular pressure at blood vessel walls, continual deformation and relaxation of the poroelastic medium leads to deformation waves that propagate and attenuate through the medium, generating transient fluid flows in response to these porosity fluctuations. Even in the simplest scenario of a one-dimensional (1D) homogeneous material under sinusoidal forcing, it has been recognized [8] that transient forcing of poroelastic materials can induce deformation and flow phenomena that do not arise in the steady counterpart. Local flows are further impacted by spatial heterogeneities—in properties such as permeability, porosity, or elasticity—that are inherent to many porous materials. In concert, the combination of transient forcing, poroelastic media, and spatial heterogeneities leads to complex fluidic transport phenomena that fundamentally differ from their steady, inelastic, or homogeneous counterparts. These characteristics (transient flow, poroelasticity, heterogeneity) arise in a variety of porous media applications, including flow and transport in biological tissues [9,10] and tissue engineering scaffolds [11,12], hydrogels [13], geological media [14], and engineered injection and extraction in compressible sediments [15,16]. One important application area is flow and transport in brain tissue [17,18], which acts as a porous medium at macroscopic length scales [19,20]. Such transport governs waste removal in the brain and is linked with a number of neurodegenerative disorders. In this context, different transient pressure forcings during REM sleep are known to significantly impact waste transport [21], however the underlying mechanisms are not well understood. In the context of mixing in coastal aquifers, several studies [22–24] have examined the impact of transient tidal forcing, spatial heterogeneity, and regional groundwater flow on solute transport in poroelastic media. While these studies observe complex flow and transport phenomena, the underlying flow kinematics were not examined.

Recent theoretical studies [6,25,26] have established that this combination of characteristics generates a rich array of complex fluidic transport that can only be properly understood in the Lagrangian frame. Conversely, these transport dynamics are impossibly complicated in the Eulerian frame, hindering insight into the underlying transport mechanisms. Using the tools and techniques of classical nonlinear dynamics and chaotic advection [27,28], it can be shown that purely advective transport in transient heterogeneous poroelastic systems is controlled by Lagrangian coherent structures (LCSs) [29], which are structures in the Lagrangian frame that arise when there are sufficient degrees of freedom in the flow. In 2D, LCSs consist of hyperbolic, parabolic, and elliptic surfaces [30] that bound chaotic regions, where fluid elements are rapidly mixed and stretched exponentially in time, and regular regions, where fluid mixing and deformation is slower (subexponential). LCSs also form transport barriers that direct and retard advective transport. Hence LCSs are fundamental to understanding advective transport in transient heterogeneous poroelastic systems.

While advective transport is relatively well understood, currently little is known regarding the transport of diffusive species such as solutes, colloids, and heat in transient poroelastic systems. In the present study, our focus is directed towards comprehending the distinct transport behaviors that emerge as diffusive solutes interact with various LCSs within the framework of driven poroelastic media. In general, LCSs govern diffusive transport via the interaction of diffusion and deformation history. For example, it is well established [30,31] that hyperbolic LCSs form transport barriers or “surfaces of minimal flux” with respect to diffusive solutes, resulting in exponentially retarded diffusion across these barriers. Hence these LCS types, along with elliptic and parabolic LCSs, organize and control diffusive solute transport.

Although LCSs can arise in both 2D and 3D flows, in this study we limit the scope to 2D systems to aid visualization of LCSs and highlight their impact on solute transport, specifically the strong departures from classical flow and transport in porous media. Certainly, 3D effects are important in many systems [29,30,32]; hence, investigation of flow and transport in 3D poroelastic flows

from a dynamical systems perspective represents a rich future research direction. Here we aim to quantify and elucidate the intricate solute transport behavior inherent to transient heterogeneous poroelastic systems, and explicitly show how these Lagrangian structures profoundly impact transport of diffusive solutes in poroelastic flows. To this end, we consider transport in a model 2D poroelastic system, a periodically forced, heterogeneous poroelastic medium (PFHPM). Although the PFHPM is relatively simple and computationally feasible, it contains the minimum ingredients (i–iii) outlined above for complex advection dynamics to arise. These dynamics manifest as a rich array of LCSs in the Lagrangian frame [29] that vary with the parameters of the PFHPM flow [26]. Our focus here is to examine the dispersion (spreading) of diffusive solutes as they migrate through the complex PFHPM flow and to relate dispersive features apparent in the solute clouds at local and global scales to the types and distributions of LCSs encountered during the migration. We note that the mixing state (or dilution [33]) of the solute plume is also an important aspect of transport [34] which may feasibly be addressed by the present approach. However, we limit the scope of the present work to consider only solute dispersion in the presence of Lagrangian coherent structures, and we defer solute mixing analysis to a later study (in preparation).

This study proceeds as follows. First, in Sec. II we introduce the conventional 2D Darcian model in [6] representing a periodically forced, heterogeneous poroelastic medium (PFHPM). This model serves as the foundation for a comprehensive Lagrangian analysis of the flow regime. In Sec. III we then present a numerical method designed to simulate a large number of diffusive particles in the PFHPM flow, and in Sec. IV we briefly review the fundamental advective dynamics governing this system that serve as a basis for understanding diffusive transport, including identification of the different LCS types that govern advective transport in the PFHPM. In Secs. V and VI, we then investigate and quantify diffusive solute transport within the different LCS types over a range of Péclet numbers ranging from pure advection to diffusion-dominated. Insights from these local analyses within each LCS type are then used to develop an understanding of global transport across the flow domain, including quantification of spatial and temporal moments, residence time distributions, and dilution indices. Finally, in Sec. VII conclusions are drawn regarding the potential implications of these findings for relevant processes that govern such PFHPM systems.

II. MODEL DESCRIPTION

A. PFHPM flow

To begin, we briefly introduce the PFHPM model that serves as a basis for investigation of diffusive transport in poroelastic systems. A more comprehensive description can be found in Refs. [6,25,26], where the PFHPM model was proposed as a simplified model of flow and transport in coastal compressible groundwater aquifers subject to a combination of a constant inland flow and oscillatory tidal forcing. In the present study, we consider the PFHPM model as an example of complex flow and transport that can arise in a generic heterogeneous poroelastic media across a wide range of applications ranging from biological systems, geophysical applications, and industrial applications. As we are primarily focused on the study of diffusive transport in heterogeneous poroelastic media, we consider the simplest possible model system that is capable of generating complex transport dynamics. As such, insights from the PFHPM model are applicable to a broad range of poroelastic applications.

As shown in Fig. 1, the PFHPM model flow consists of a 2D compressible heterogeneous porous medium at the Darcy scale in the square domain $\mathcal{D} : \mathbf{x} = (x, y) \in [0, L] \times [0, L]$ with a heterogeneous conductivity field $K(\mathbf{x})$ that is driven by pressure boundary conditions at $x = 0$ (oscillatory) and $x = L$ (steady). Here we only consider one realization of this log-Gaussian random field, but in a previous study [26] we show that different realizations generate similar overall transport characteristics. Although many poroelastic systems possess complex constitutive behavior, for simplicity we consider the solid matrix simply to be linearly poroelastic in that it undergoes reversible compression in response to changes in local fluid pressure, where the local porosity φ

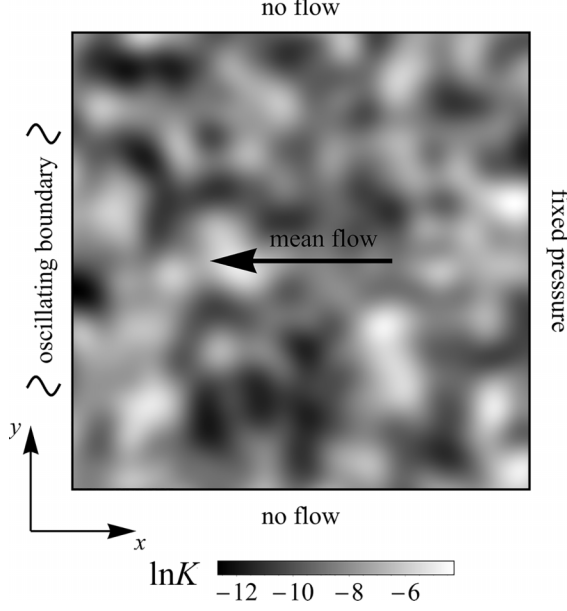


FIG. 1. Schematic of the PFHPM 2D model domain indicating the mean flow direction, pressure boundary conditions and heterogeneous conductivity field. The gray-scale shading indicates the value of the log-conductivity field $\ln K(\mathbf{x})$.

varies linearly with fluid pressure as

$$\varphi(p) = \varphi_{\text{ref}} + S(p - p_{\text{ref}}), \quad (1)$$

where S is the (constant) compressibility of the solids matrix with units of inverse pressure; φ_{ref} and $p_{\text{ref}} = 0$ are the reference porosity and pressure, respectively. Note that for some applications such as groundwater flow in aquifers, the solid phase is incompressible but the solids matrix may still undergo displacement due to changes in the local pore pressure, resulting in evolution of the compressibility. Although the behavior of such incompressible yet deformable solids is described by the solids continuity equation subject to appropriate closures, to leading order their behavior is still modeled as per Eq. (1).

The resultant Darcy flux vector field $\mathbf{q}(\mathbf{x}, t)$ is given by the Darcy equation

$$\mathbf{q}(\mathbf{x}, t) = -K(\mathbf{x})\nabla p(\mathbf{x}, t), \quad (2)$$

where the heterogeneous conductivity field $K(\mathbf{x})$, with units of length squared per unit time multiplied by inverse pressure, satisfies $K = k/\mu$, where k is the intrinsic permeability distribution within the model domain, and μ is the dynamic viscosity of the fluid, assumed constant. Henceforth, we will refer to K in all analysis; K is modeled as a log-Gaussian random spatial function with mean K_{eff} , log-variance $\sigma_{\ln K}^2$, and correlation length ℓ . Note that while the medium is compressible, for simplicity the medium conductivity is considered to be steady. The fluid pressure field $p(\mathbf{x}, t)$ satisfies the no-flux boundary conditions

$$\frac{\partial p}{\partial y}\bigg|_{y=0} = \frac{\partial p}{\partial y}\bigg|_{y=L} = 0 \quad (3)$$

and the fixed and oscillatory boundary conditions

$$p(L, y, t) = JL, \quad p(0, y, t) = g(t), \quad (4)$$

where the mean pressure gradient J generates a mean flow from right to left, and the oscillatory forcing function

$$g(t) = g_p \sin \omega t \quad (5)$$

has zero mean with amplitude g_p , period P , and frequency $\omega \equiv 2\pi/P$. The pressure field p decomposes into steady (p_s) and periodic (p_p) components as

$$p(\mathbf{x}, t) = p_s(\mathbf{x}) + p_p(\mathbf{x})e^{i\omega t}, \quad (6)$$

where $p_s(\mathbf{x})$ also corresponds to the steady case $g(t) = 0$.

Across various poroelastic applications, this fluctuating pressure boundary condition may arise from hydrological (e.g., tidal, seasonal, climatic), biophysical (e.g., blood pressure, pulmonary), or engineered fluctuations, the simplest functional form of which is the sinusoidal function $g(t)$. Trefry *et al.* [6] show that interactions between the unsteady flow generated by the forcing function $g(t)$ and the steady flow associated with the mean pressure gradient J over the domain lead to intricate advective dynamics that do not arise in either the homogeneous, steady, or incompressible counterparts to the PFHPM flow. Hence, the PFHPM model represents the simplest such flow that exhibits advective complexity.

In conjunction with the continuity equation for the fluid phase [35]

$$\frac{\partial \varphi}{\partial t} + \nabla \cdot \mathbf{q} = 0, \quad (7)$$

the Darcy (2) and constitutive (1) equations lead to the governing pressure equation [6,35]

$$S \frac{\partial p}{\partial t} = \nabla \cdot [K(\mathbf{x}) \nabla p(\mathbf{x}, t)], \quad (8)$$

subject to the boundary conditions (3) and (4). From (8), the steady p_s and periodic p_p pressure components satisfy

$$\nabla \cdot [K \nabla p_s(\mathbf{x})] = 0, \quad (9)$$

$$\nabla \cdot [K \nabla p_p(\mathbf{x})] - i\omega S p_p(\mathbf{x}) = 0, \quad (10)$$

which quantifies the porosity $\varphi(\mathbf{x}, t)$ and Darcy flux $\mathbf{q}(\mathbf{x}, t)$ via Eqs. (1) and (2), respectively. To highlight the impact of oscillatory forcing upon solute transport, we also examine transport in the steady analog (SHPM) of the PFHPM flow using the steady pressure field p_s that corresponds to $g(t) = 0$ as a reference case. The corresponding steady porosity $\varphi_s(\mathbf{x})$ and steady Darcy flux vector field $\mathbf{q}_s(\mathbf{x})$ are given, respectively, by Eqs. (1) and (2).

B. Solute transport

To examine purely advective solute transport, the position \mathbf{x} of nondiffusive solute particles evolves via the advection equation

$$\frac{d\mathbf{x}}{dt} = \mathbf{v}(\mathbf{x}, t), \quad \mathbf{x}(t_0) = \mathbf{x}_0, \quad (11)$$

where the fluid velocity field $\mathbf{v}(\mathbf{x}, t)$ is related to the Darcy flux $\mathbf{q}(\mathbf{x}, t)$ as

$$\mathbf{v}(\mathbf{x}, t) = \frac{\mathbf{q}(\mathbf{x}, t)}{\varphi(\mathbf{x}, t)}. \quad (12)$$

For diffusive solute transport (ignoring velocity-dependent anisotropic dispersion for simplicity), the position \mathbf{x} of a diffusive solute tracer particle evolves according to the Langevin equation

$$\frac{d\mathbf{x}}{dt} = \mathbf{v}(\mathbf{x}, t) + \sqrt{2D_m} \boldsymbol{\xi}(t), \quad \mathbf{x}(t_0) = \mathbf{x}_0, \quad (13)$$

where D_m is the molecular diffusivity of the solvent, and $\xi(t)$ is a Gaussian noise vector with zero mean $\langle \xi(t) \rangle = \mathbf{0}$ and unit variance and is δ -correlated in time as $\langle \xi(t) \xi(t') \rangle = \delta(t - t') \mathbf{I}$. The corresponding Fokker-Planck equation for the concentration field $c(\mathbf{x}, t)$ field of an ensemble of solute particles is given by the advection-diffusion equation (ADE)

$$\frac{\partial c}{\partial t} + \nabla \cdot [\mathbf{v}(\mathbf{x}, t)c] - D_m \nabla^2 c = 0, \quad c(\mathbf{x}, 0) = c_0(\mathbf{x}), \quad (14)$$

where c refers to the solute mass per unit volume of a *porous matrix*. For comparison, the ADE for the concentration field $C(\mathbf{x}, t)$ corresponding to the solute mass per unit volume of *fluid* in the pore space is [35]

$$\frac{\partial}{\partial t}(C\varphi) + \nabla \cdot (C\varphi \mathbf{v}) - \nabla \cdot (\varphi D_m \nabla C) = 0, \quad C(\mathbf{x}, 0) = C_0(\mathbf{x}), \quad (15)$$

where $c(\mathbf{x}, t) \equiv C(\mathbf{x}, t)\varphi(\mathbf{x}, t)$ and $c_0(\mathbf{x}) = C_0(\mathbf{x})\varphi(\mathbf{x}, 0)$. Under the assumption that spatial gradients of the porosity field φ are small compared to those of the concentration field C , i.e., $|\varphi \nabla C| \gg |C \nabla \varphi|$ (see Appendix A for details), then the ADE (15) is equivalent to (14). Note that from (14), nondiffusive solute particles that are advected via (11) are representative of the concentration field c .

C. Dimensionless equations and parameter groups

The preceding equation system may be placed in nondimensional form via scaling analysis as detailed in Appendix B. Note that due to the presence of diffusive solute transport, the scalings that are applied here are different from those in previous studies [6,25,26], leading to altered definitions for some dimensionless parameters.

Previous works [6,25,26] used the domain size L and forcing period P as length and time scales for rescaling the advective PFHPM problem. In the present work, which is focused on diffusive transport through the heterogeneous medium, we choose the correlation length scale ℓ of the conductivity field $K(\mathbf{x})$ as the characteristic length scale, as the heterogeneities in $K(\mathbf{x})$ on this length scale generate the vorticity that produces transport complexity in the PFHPM flow. Time is then nondimensionalized with respect to the advection time $\tau_a = \ell/V_{\text{eff}}$ over a correlation length, where $V_{\text{eff}} = JK_{\text{eff}}/\varphi_{\text{ref}}$ is the mean Darcy flow velocity through the domain induced by the pressure gradient J . In addition to these scalings, pressure is nondimensionalized as $p' = p/(J\ell)$, velocity as $\mathbf{v}' = \mathbf{v}/V_{\text{eff}}$, hydraulic conductivity as $\kappa(\mathbf{x}) = K(\mathbf{x})/K_{\text{eff}}$, porosity as $\varphi' = \varphi/\varphi_{\text{ref}}$, and solute concentration as $c' = c/c_{\text{max}}$, where c_{max} is the maximum concentration of the initial condition $c_0(\mathbf{x})$. Full details regarding these choices are provided in Appendix B. These choices then permit the governing equations to be cast in dimensionless form by dropping the primes as follows. The rescaled constitutive equation becomes

$$\varphi = 1 + \frac{C}{\mathcal{G}}p, \quad (16)$$

the nondimensional governing equations for the steady and periodic pressure components are

$$\nabla \cdot [\kappa \nabla p_s(\mathbf{x})] = 0, \quad (17)$$

$$\nabla \cdot [\kappa \nabla p_p(\mathbf{x})] - i\mathcal{T}p_p(\mathbf{x}) = 0, \quad (18)$$

with dimensionless boundary conditions

$$p_s(0, y) = 0, \quad p_s(L/\ell, y) = L/\ell, \quad (19)$$

$$p_p(0, y) = \mathcal{G}, \quad p_p(L/\ell, y) = 0, \quad (20)$$

TABLE I. Dimensionless parameters for PFHPM flow.

Parameter	Symbol	Definition	Value
Townley number	\mathcal{T}	$\ell^2 S\omega/K_{\text{eff}}$	0.0754
Forcing strength	\mathcal{G}	$g_p/J\ell$	204.1
Compression ratio	\mathcal{C}	$Sg_p/\varphi_{\text{ref}}$	0.5
Péclet number	Pe	$V_{\text{eff}}\ell/D_m$	$86.4 - \infty$
Dimensionless forcing period	P'	P/τ_a	0.204
Conductivity log-variance	$\sigma_{\ln \kappa}^2$		2
Dimensionless domain size	L'	L/ℓ	20.4

and the nondimensional ADE (14) then takes on the standard form

$$\frac{\partial c}{\partial t} + \nabla \cdot [\mathbf{v}(\mathbf{x}, t)c] - \frac{1}{\text{Pe}} \nabla^2 c = 0, \quad c(\mathbf{x}, 0) = c_0(\mathbf{x}). \quad (21)$$

The resultant parameter groups are summarized in Table I; see Appendix B for details. Of these, four dimensionless parameters form the main parameter set $\mathcal{Q} = (\mathcal{T}, \mathcal{C}, \mathcal{G}, \text{Pe})$ that governs solute transport and mixing in the PFHPM flow. The compression ratio \mathcal{C} characterizes the porosity change associated with the oscillatory pressure amplitude g_p as

$$\mathcal{C} = \frac{Sg_p}{\varphi_{\text{ref}}}. \quad (22)$$

The forcing strength \mathcal{G} characterizes the strength of the oscillatory pressure amplitude relative to the mean pressure gradient over a correlation length ℓ as

$$\mathcal{G} = \frac{g_p}{J\ell}. \quad (23)$$

The Townley number \mathcal{T} characterizes the ratio of the attenuation length scale l_a of the oscillatory pressure signal to the characteristic length scale ℓ as

$$\mathcal{T} = \frac{\ell^2}{l_a^2} = \frac{\ell^2 S\omega}{K_{\text{eff}}}. \quad (24)$$

The Péclet number Pe which characterizes the relative time scales of advection $\tau_a = \ell/V_{\text{eff}}$ to diffusive $\tau_d = \ell^2/D_m$ solute transport is

$$\text{Pe} = \frac{\tau_d}{\tau_a} = \frac{V_{\text{eff}}\ell}{D_m} = \frac{JK_{\text{eff}}\ell}{\varphi_{\text{ref}}D_m}. \quad (25)$$

The additional independent physical parameters that completely define the PFHPM flow are the log-variance $\sigma_{\ln \kappa}^2 = \sigma_{\ln \kappa}^2$ of the hydraulic conductivity field $\kappa(\mathbf{x})$ and the forcing period $P = 2\pi/\omega$.

D. Parameter values and ranges

In Ref. [26] we considered how the advective transport dynamics of the PFHPM flow alter over the parameter space $(\mathcal{T}, \mathcal{C}, \mathcal{G})$. In this study, we choose fixed values of these parameters that give rise to a wide range of LCSs in the flow domain, and we consider the impact of these structures upon diffusive solute transport by varying Pe. As indicated in Table I, the chosen dimensionless parameters in this study include the Townley number $\mathcal{T} = 0.0754$, forcing amplitude $\mathcal{G} = 204.1$, and compression ratio $\mathcal{C} = 0.5$. The \mathcal{G} and \mathcal{C} values are deliberately chosen to accentuate the compressible influence, facilitating a more systematic investigation into the interplay between diffusive solute plumes and Lagrangian coherent structures. The log-conductivity variance $\sigma_{\ln \kappa}^2 = 2$

is chosen to represent transport in a moderately heterogeneous medium, and the dimensionless forcing period $P' = 0.204$ scales from an earlier choice of $P = 1$ d for a diurnal tidal context [6].

The Péclet number is varied over the values $Pe = 86.4, 864, 8640$, which range from diffusion-dominated to advection-dominated transport, and the purely advective dynamics $Pe = \infty$ are also considered. Although this Péclet number range may not encompass all possible values, it remains relevant and applicable to a wide range of physical systems. For completeness, a list of the corresponding dimensional parameters for a typical bench-top experiment is given in Table II in Appendix B. Using the corresponding dimensionless parameter values in Table I, a 164×164 finite-difference grid over the 2D unit square \mathcal{D} is used to solve the dimensionless steady and periodic pressure fields governed by (17) and (18), from which the porosity, velocity, and Darcy flux vector fields are subsequently calculated as described in previous works [6,36].

III. METHODOLOGY

The study of transport dynamics in complex flows requires the development of suitable numerical methods to accurately track particles and visualize the associated LCSs. Additional methods are also required to accurately simulate diffusive solute transport. To address these needs, our research focuses on two key methodologies: (i) the particle mapping method (PMM) for efficient and accurate particle tracking and LCS identification, and (ii) the diffusive mixing method (DMM) for simulation of diffusive solute transport. We outline these methods as follows.

A. Particle mapping method

In a previous study [6], we proposed a mapping method to rapidly advect particles in 2D time-periodic flows based on approximation of the map $\Phi(\mathbf{x}_0, t_0, t) = \mathbf{x}(t)$ for a particle initially at position \mathbf{x}_0 at time $t = t_0$, which is the formal solution to the advection equation (11), where the flow velocity \mathbf{v} is P' -periodic in time, i.e., $\mathbf{v}(\mathbf{x}, t + P') = \mathbf{v}(\mathbf{x}, t)$. The “single-step” variant of this method is based upon numerical approximation of the flow map $\Phi(\mathbf{x}_0, 0, P')$ over one period P' of the flow via the solution of the advection equation (11) over an evenly spaced $N_{\text{grid}} \times N_{\text{grid}}$ grid of initial points $\mathbf{x}_{0,i}$ that spans the flow domain \mathcal{D} . The interpolated map

$$\hat{\Phi}(\mathbf{x}_0) \approx \Phi(\mathbf{x}_0, 0, P') \quad (26)$$

for the particle position at $t = P'$ is then constructed for an arbitrary initial position \mathbf{x}_0 via interpolation of the grid-based values $\Phi(\mathbf{x}_{0,i}, 0, P')$. The resultant interpolated map can then be used to rapidly advect particles over many flow periods as

$$\mathbf{x}_{n+1} = \hat{\Phi}(\mathbf{x}_n), \quad (27)$$

where \mathbf{x}_n is the particle position at $t = nP'$ for $n = 0, 1, \dots$. This approach alleviates the need to repeatedly solve the advection equation (11), and numerical testing, which has been validated against numerical solutions of the advection equation (11), suggests small relative L_2 errors (order 10^{-3} [6,26]) in the particle advection can be achieved with sufficient resolution ($N_{\text{grid}} \sim 400$) of the flow domain.

B. Diffusive mapping method

In this study, the PMM is extended to approximate solute advection-diffusion via operator splitting of the dimensionless form of the Langevin equation (13). This method was not tested against the Langevin equation (13) directly, but rather was validated against the finite-element method (FEM) in Appendix C. By splitting the diffusion step into two half-steps before and after the advection step, the position of a diffusive solute particle can be updated over one period P as

$$\mathbf{x}_{n+1} = \hat{\Phi}(\mathbf{x}_n + \sqrt{P'/Pe} \boldsymbol{\xi}) + \sqrt{P'/Pe} \boldsymbol{\xi}, \quad (28)$$

where ξ is a vector comprised of two independent Gaussian random variables with zero mean and unit variance. As diffusive solute transport is dependent upon fluid deformation history [37], operator splitting of advection and diffusion over the flow period P' is found to be too coarse for accurate simulation, hence it is necessary to resolve fluid advection on a time scale finer than P' . As such, the time step $\delta t = P'/N_{\text{step}}$ for some integer $N_{\text{step}} > 1$ is used as a basis for operator splitting (see Appendix C for details), based on the advective map

$$\hat{\Phi}_m(\mathbf{x}_0) \equiv \Phi(\mathbf{x}_0, m\delta t, (m+1)\delta t), \quad m = [0 : N_{\text{step}} - 1], \quad (29)$$

which maps the position of a tracer particle at \mathbf{x}_0 at time $t = m\delta t$ forward in time by δt . In combination with half-step diffusion operator splitting, the position of a solute particle is then updated via the diffusive mapping method (DMM) as

$$\mathbf{x}_{m+1} = \hat{\Phi}_{\text{mod}(m, N_{\text{step}})}(\mathbf{x}_m + \sqrt{\delta t/\text{Pe}} \xi) + \sqrt{\delta t/\text{Pe}} \xi. \quad (30)$$

In Appendix C, this operator-splitting solution method is verified against independent numerical computations using a finite-element method. Various splitting methods and temporal discretizations (characterized by N_{step}) are considered in Appendix C, where it was found that $N_{\text{step}} = 32$ and the half-step operator splitting method were optimal for accurate simulation of diffusive solute transport.

IV. ADVECTIVE DYNAMICS OF THE PFHPM

Although previous studies [6,25,26] have investigated purely advective solute transport in the PFHPM flow, we provide a brief review here to establish the context for investigation of diffusive solute transport. This includes a brief review of the fundamental concepts and findings from these previous studies regarding Lagrangian transport in the PFHPM flow. In addition to this brief review, we also conduct a fluid stretching analysis to gain an understanding of advective solute transport across the flow domain. Resolving these advection dynamics and the associated transport structures (LCSs) forms the basis for investigating and understanding the complex interplay between advection and diffusion, which is undertaken in Sec. V.

A. Advective solute transport

To visualize advective transport in the PFHPM flow, we consider four distinct initial solute blob locations (denoted as A, B, C, D) near the interior (right-hand) boundary of the flow domain, as shown in Fig. 2 (bottom). As shall be shown, these initial blob locations were chosen to illustrate and investigate interaction of the evolving blobs with different LCSs in the flow domain. For these advection-only simulations, the solute blobs are comprised of $N_p = 10^5$ tracer particles, which are initialized according to a symmetric 2D Gaussian distribution with standard deviation $\sigma = 1.25 \times 10^{-3}L$ centered on the specified initial locations A–D.

Many analytical solutions have been reported for the pressure profile in compressible low-dimensional porous media subjected to time-periodic forcing, for homogeneous (see, e.g., [38–40]) and for structured and heterogeneous (see, e.g., [41,42]) systems. Figure 2 (top) shows the exponential decay of the normalized pressure fluctuation $|p_p(x)/\mathcal{G}|$ with spatial coordinate x in a homogeneous medium ($\sigma_{\ln K}^2 = 0$), highlighting attenuation of the pressure fluctuation away from the periodic boundary. As shown, the attenuation length scale is governed by the Townley number \mathcal{T} , and is negligible at the domain boundary $x = L/\ell$. The region ($x\ell/L < 0.5$) of significant pressure fluctuations has been found [6] to correspond with regions of complex transport dynamics in the PFHPM flow domain, illustrating the significance of periodic flow upon complex transport phenomena. This correspondence is reflected in Fig. 2 (bottom), which shows the complete trajectories of several solute tracer particles (in the absence of diffusion) released at locations A–D for both the periodically forced flow (colored trajectories) and the corresponding steady flow (black trajectories). On the right-hand side (RHS) of the flow domain, the impact of the pressure oscillations upon

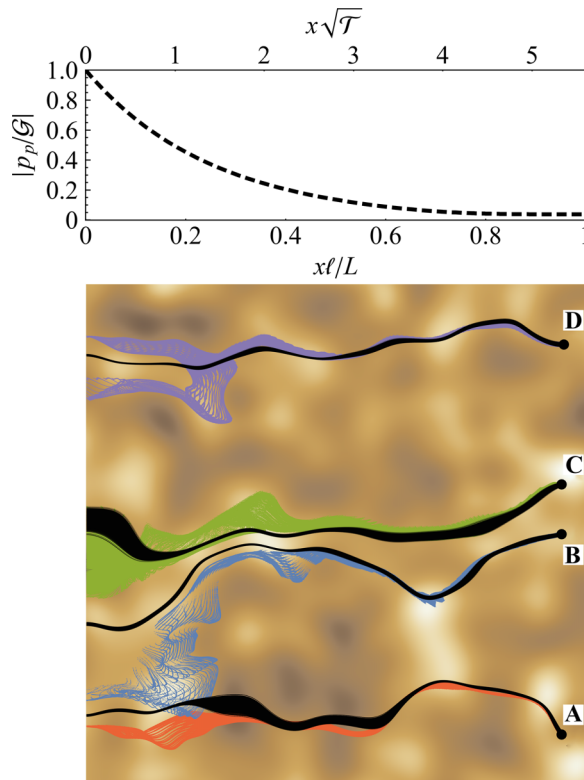


FIG. 2. Pressure profiles and flow paths in the PFHPM and SHPM flows. Top: The dashed curve illustrates exponential decrease of the normalized amplitude of the pressure fluctuation ($|p_p/G|$) for the equivalent homogeneous case. The upper axis is rescaled in terms of the dissipation length $x\sqrt{\mathcal{T}}$. Bottom: Flow paths of several tracer particles that comprise the four solute blobs originating at initial locations A, B, C, and D in the (black) steady flow and (colored) periodic flow. The tracer particle positions are plotted at intervals of $\delta t = P'/32$. Note that the black circular symbols at the initial locations A, B, C, D are significantly larger than the initial solute blob size.

advective transport is minimal, and the tracer particles in the steady and periodic flows follow similar trajectories. Conversely, as these particles move toward the forcing boundary [and the magnitude of the pressure oscillation becomes significant, as indicated in Fig. 2 (top)], advective transport is markedly different, with tracer particles in the oscillatory flow making spiral orbits along significantly different trajectories from that of the steady flow. Animations of the advective blob evolution in the steady and periodic flows are also shown in the supplemental material [43] as Movies S1–S2. Overall, there exist three distinct differences between the advective transport dynamics in the steady and periodically forced flows:

Intraperiod oscillations. For the periodic flow, tracer particles exhibit oscillatory behavior within each flow period as they traverse the flow domain. This characteristic is more pronounced in the vicinity of the forcing boundary and is particularly clear in the animations in the supplemental material [43]. Although these oscillations do persist far from the forcing boundary, in this region they tend to be confined to coherent “streamlines” and so net (interperiod) transport is not significantly different from the steady flow.

Onset of complex transport dynamics. As tracer particles get closer to the forcing boundary in the periodic flow, these intraperiod oscillations become larger and also exhibit symmetry-breaking, resulting in particle trajectories that are not confined to coherent “streamlines.” This manifests as

the spiralling particle trajectories shown near the forcing boundary in Fig. 2 (bottom), and complex net transport dynamics.

Emergence of trapped regions. In addition to complex orbits, there also exist regions [not readily apparent in Fig. 2 (bottom)] of the periodic flow near the forcing boundary that contain “trapped” tracer particles that stay within these regions indefinitely. Conversely, such trapping is not possible in the steady flow, and all tracer particles exit the flow domain in finite time.

These fundamental differences arise from the additional degree of freedom (DOF) imparted by the periodically forced flow. As the steady 2D flow has $\text{DOF} = 2$ (corresponding to the two spatial dimensions), chaotic advection is not possible as per the Poincaré-Bendixson theorem. Conversely, the addition of a further temporal DOF in the PFHPM flow ($\text{DOF} = 3$) admits the possibility of chaotic advection. In addition to such periodic forcing, in [6] we showed that the necessary ingredients for chaotic advection in the PFHPM flow are heterogeneity of the hydraulic conductivity field and compressibility of the porous medium. The former of these ingredients is necessary for the generation of vorticity (and hence homoclinic and heteroclinic tangles, the hallmark of chaotic dynamics), while the latter is necessary for the formation of open-particle trajectories that are not confined to coherent “streamlines” (leading to complex particle transport).

B. Stretching analysis

Due to the complexity of the orbits shown in Fig. 2, merely examining the particle trajectories is insufficient to fully elucidate the underlying structures that govern solute transport and mixing behavior. Hence it is necessary to eliminate the influence of intraperiod particle dynamics and focus on interperiod motions to gain a clearer understanding of the underlying structure. We employ a dynamic tool known as the Poincaré section to accomplish this objective. The Poincaré section acts as a stroboscopic map, capturing the location of advected particles at each flow period P' . By utilizing the Poincaré section, we can effectively analyze the interperiod behavior of tracer particles and help identify the LCSs that influence both purely advective transport and transport of diffusive solutes.

In previous studies [6,26], various LCS types in the PFHPM flow were identified. In this study, we extend this analysis by demarcating the regions of the flow domain that correspond to various LCS types. In addition to the Poincaré section, analysis of fluid deformation within the PFHPM flow is also necessary to identify these LCS types and their corresponding regions. Regions of regular or chaotic fluid advection (which correspond to different classes of LCS) can be identified, respectively, by the absence or presence of fluid deformation that evolves exponentially in time. Hence the characteristic stretching exponent for a given region, known as the Lyapunov exponent λ , serves as an indicator for regular ($\lambda = 0$) or chaotic ($\lambda > 0$) advection. For closed flows, regular and chaotic regions can be distinguished by computing the infinite-time Lyapunov exponent in each distinct region of the Lagrangian topology as

$$\lambda_{\infty} = \lim_{(t-t_0) \rightarrow \infty} \frac{1}{2(t-t_0)} \ln v(\mathbf{X}, t_0, t), \quad (31)$$

where $v(\mathbf{X}, t_0, t)$ is the largest eigenvalue of the Cauchy-Green deformation tensor $C(\mathbf{X}, t_0, t)$ for a tracer particle with initial position \mathbf{X} at time t_0 (a detailed description is in Ref. [6], Appendix D). Here the infinite-time Lyapunov exponent is constant in space throughout each distinct region due to the ergodicity of particle trajectories in chaotic domains, while it is everywhere zero in regular regions.

However, this approach becomes impractical for open flows such as the PFHPM flow since fluid elements traverse the flow domain in finite time, preventing the computation of an infinite-time Lyapunov exponent. To overcome this challenge, the finite-time Lyapunov exponent (FTLE) can be used to analyze the stretching dynamics over the finite time interval $t - t_0$ as

$$\lambda(\mathbf{X}, t_0, t) = \frac{1}{2(t-t_0)} \ln v(\mathbf{X}, t_0, t). \quad (32)$$

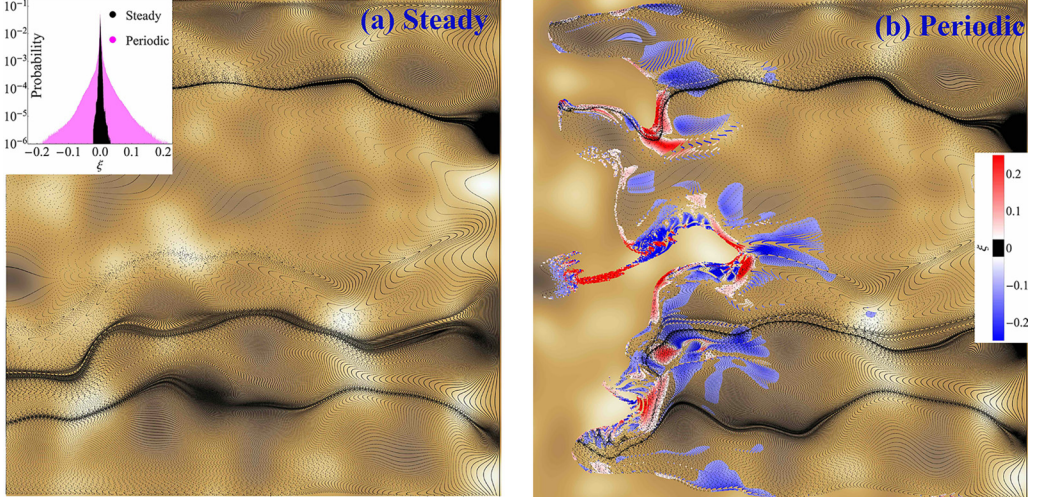


FIG. 3. Relative stretching $\xi_i(t)$ in (a) steady and (b) periodic two-dimensional heterogeneous poroelastic Darcy flow with conductivity field correlation length $\ell = 0.049$. Left inset: Probability density function of ξ_i from an ensemble of 75 million variates $\xi_i(t_j)$ calculated from 2×10^4 tracer particles with time increments $\delta t = P'/32$. Tracer particles are colored according to the local value of ξ as per the legend (bottom right inset), where particles with local compression (blue) and stretching (red) greater than the threshold magnitude $|\xi| > \xi_{\text{crit}}$ are colored with larger stretching magnitudes depicted by more intense colors.

The FTLE is related to the finite-time stretching exponent (FTSE) ξ of a material line over the time period δt by

$$\xi_i(t) = \frac{1}{\delta t} \ln \frac{e_i(t + \delta t)}{e_i(t)}, \quad (33)$$

where $e_i(t) = \|\mathbf{x}_i(t) - \mathbf{x}_{i+1}(t)\|$ is the distance at time t between a pair of tracer particles with respective current locations $\mathbf{x}_i(t)$, $\mathbf{x}_{i+1}(t)$. From (32) and (33), the FTLE $\lambda(\mathbf{X}, t, t + \delta t)$ is equivalent to the maximum (with respect to all orientations) of $|\xi_i(t)|$ for an infinitesimally spaced pair of particles at position \mathbf{X} . As such, the FTSE magnitude $|\xi|$ serves as a useful low-order approximation of the FTLE.

To quantify fluid stretching in both the PFHPM and SHPM flows, a series of tracer particles with initial locations $\mathbf{x}_i(0) = (0.995L/\ell, i/IL/\ell)$, $i = 1 : I$, $I = 2 \times 10^4$ are advected through the flow domain. From (33), the FTSEs arising from fluid stretching between these tracer particles are computed, where positive values of ξ_i correspond to stretching of line elements and negative values correspond to compression. We find that the time increment $\delta t = P'/32$ for the FTSE represents a suitable compromise between averaging of velocity fluctuations and finite residence time. From the histogram of stretching exponents $\xi_i(t)$ for the steady flow shown in Fig. 3 (top, inset), the FTSE is bound by the threshold $|\xi_i(t)| < \xi_{\text{crit}} \approx 0.025$.

As the steady flow must be nonchaotic, we define line stretching/compression exponents greater than this threshold $|\xi_i(t)| > \xi_{\text{crit}}$ to be representative of regions of chaotic advection. As such, the regions associated with strong stretching/compression [i.e., $|\xi_i(t)| > \xi_{\text{crit}}$] in Fig. 3 (bottom) are considered to be associated with chaotic advection, whereas weaker deformation regions are considered to be nonchaotic. Although this demarcation is indicative and not completely objective, we find that this characterization is consistent with observations of advective transport across the flow domain of the PFHPM flow.

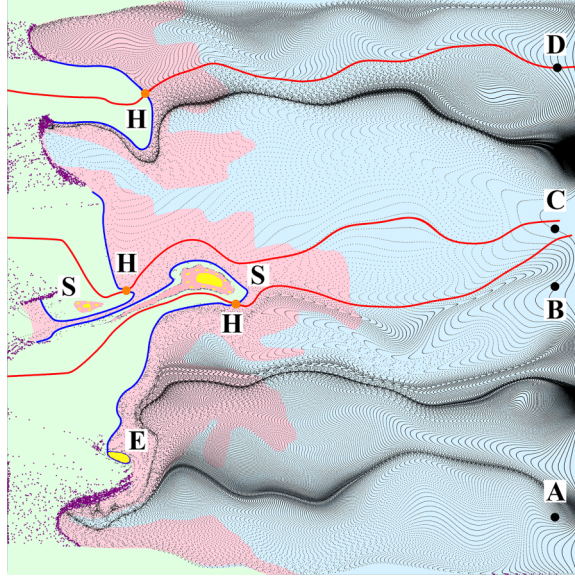


FIG. 4. Annotated and colored Poincaré section of the PFHPM flow constructed by showing fluid tracer particle positions at integer multiples of the forcing period P' . Various LCS types are shown corresponding to (i) regular region (light blue), (ii) KAM islands (light yellow), (iii) stochastic/chaotic regions (S, light pink, see text), hyperbolic points (H, orange dots), elliptic points (E), stable (red lines) and unstable (blue lines) manifolds, and the emptying region (light green). The unstable manifolds form part of the boundary of the emptying region, and the remainder of this boundary is comprised of “discharge regions” where tracer particles can flow through to the emptying region. Discharge points (purple) indicate the position of fluid tracer particles being advected through the emptying region at integer multiples of $P'/10$. Regions of the forcing boundary with (without) purple discharge points indicate punctuated “outflow” (“inflow”) regions on this boundary where fluid flows out (in) during a forcing period.

C. Identification and classification of LCSs

From the Poincaré section and stretching analysis presented in Sec. IV B, the various LCS regions in the PFHPM flow were identified, including stochastic/chaotic regions that satisfy the stretching criterion $|\xi_i(t)| > \xi_{\text{crit}}$. Figure 4 shows the Poincaré section of the PFHPM flow under consideration in this study, where the various LCSs are colored according to type, including the regular region (light blue), hyperbolic points (orange dots), KAM islands (light yellow), stochastic/chaotic regions (light pink), emptying boundary (blue), and emptying region (light green). We note that the LCS regions identified in this study are only indicative, and so the boundaries between LCS types are approximate.

The four initial locations A–D shown in Figs. 2 and 4 were chosen to investigate the solute interaction with different LCS types and gain a comprehensive understanding of their effects upon transport of diffusive solutes. Location A represents particles that solely traverse the regular and emptying regions, while location B provides an opportunity for interaction with the KAM island. Similarly, particles originating from locations B and C have the chance to enter the stochastic/chaotic region. Location D corresponds to the starting point on a stable manifold associated with a hyperbolic point, resulting in particles hitting the hyperbolic point as they approach the oscillating pressure boundary. Through these deliberately chosen initial locations, our study aims to elucidate the influence of different LCSs on solute transport and mixing dynamics in the PFHPM system, particularly when diffusion is considered.

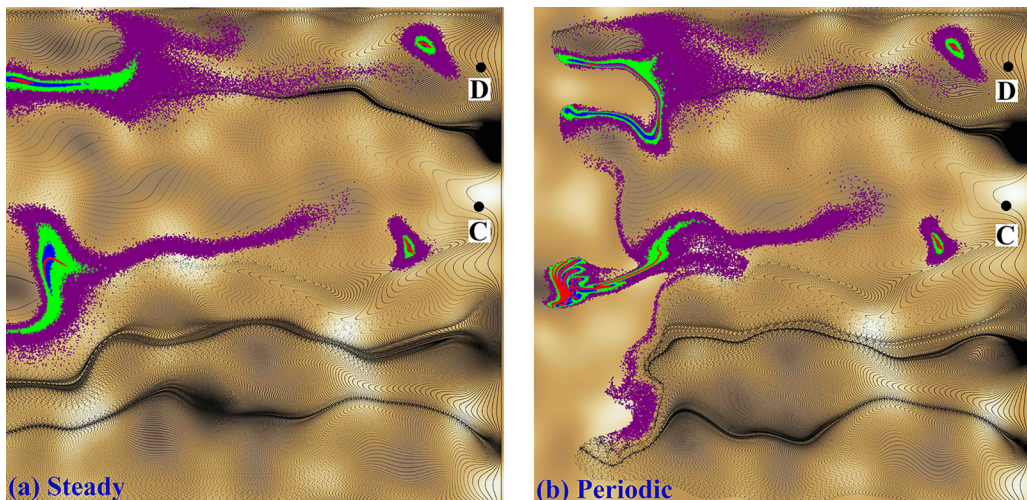


FIG. 5. Evolution of solute plumes comprised of $N_p = 10^5$ tracer particles released from initial locations C and D in (a) steady and (b) periodic flow. In each plate, the solute plumes are shown at two different times that vary with injection location: location C at $t/P' = 8, 42$ and location D at $t/P' = 12, 72$. Different tracer colors correspond to different Péclet numbers, ranging from ∞ (red), 8640 (blue), 864 (green), to 86.4 (purple).

V. LOCAL SOLUTE TRANSPORT WITHIN DIFFERENT LCS TYPES

In this section, we explore the impact of the different LCSs upon diffusive solute transport in the PFHPM flow. Our primary objective is to provide qualitative pictures that illustrate the diverse scenarios in which diffusive solutes interact with different LCS types. These qualitative depictions serve as a foundation for a subsequent quantitative analysis in Sec. VI, where we will quantify the extent and impact of global solute transport across multiple LCSs.

We inject $N_p = 10^5$ solute tracer particles at initial positions A–D in the flow domain for different Péclet numbers $Pe = 86.4 - \infty$ to uncover the interplay between solute diffusion and LCS type that governs solute transport. Figure 5 shows the evolution of diffusive solute particles originating at locations C and D for different Péclet numbers Pe in both the steady and periodic flows. See Figs. S1 and S2 in the supplemental material [43] for similar plots for initial locations A and B. Initial locations C and D involve interaction of the diffusive solute plumes with different LCS types in the flow domain. Animations of the evolution of the diffusive blobs are also available as movies S3–S6 in the supplemental material [43]. We summarize the characteristic solute transport phenomena observed within each LCS type as follows:

Regular region. As expected, evolution of diffusive solutes in the regular region of the periodic flow is very similar to that of the steady flow. Indeed, solute transport in 2D steady flow is characterized by the regular advection dynamics; in this flow, LCS types other than regular regions are not possible. In both cases, the impact of compression of the medium is minimal, and in the regular region of the periodic flow the impact of transient forcing is minimal. In both cases, as the Péclet number decreases, diffusive growth of the solute blobs increases, leading to diffusion of solute particles into low conductivity regions and stretching of the blob due to these variations in advective velocity. Hence transport of the solute blob in the regular region is dominated by velocity fluctuations mediated by heterogeneity of the porous medium.

KAM islands. In the advection-only case, the boundaries of KAM islands act as impenetrable barriers to transport that either exclude solute particles or trap them indefinitely [6]. Conversely, for solutes with finite diffusivity, KAM islands act as regions of slow transport, where solute particles are advected around the central elliptic point of the island while simultaneously diffusing normal to

the flow direction. As such, KAM islands tend to trap particles on the (dimensional) diffusive time scale $\tau_d = L_{\text{KAM}}^2/D_m$, where L_{KAM} is the characteristic size of the KAM island.

Stochastic/chaotic regions. The stochastic/chaotic regions associated with chaotic advection shown in Fig. 5 (bottom) correspond with the large stretching/compression regions shown in Fig. 3 (bottom). Upon contact with the stochastic/chaotic region, the solute blob is mixed rapidly throughout this region, leading to the iterated stretching and folding patterns shown in the middle left of Fig. 5 (bottom). Conversely, the nondiffusive solute plume in the same region of the steady flow experiences minimal stretching.

Hyperbolic points and unstable manifolds. As shown in Fig. 4, the initial location D in the flow domain is situated on the stable manifold associated with the uppermost hyperbolic point H. The unstable and stable manifolds associated with this hyperbolic point have a profound effect on solute transport. As the solute blob originating at location D reaches the hyperbolic point, it bifurcates along the two unstable manifolds emanating from the hyperbolic point without appreciably crossing them, even at lower Péclet numbers. Hence the unstable manifolds govern the ultimate trajectories of diffusive solute blob particles.

Retardation of diffusive transport across the unstable manifolds associated with this hyperbolic point can be shown explicitly by consideration of the effective dispersion local to the hyperbolic point. The ADE (14) in Lagrangian coordinates \mathbf{X} is of the form [44]

$$\frac{\partial c}{\partial t} - \nabla_{\mathbf{X}} \cdot [\mathbb{D}_0 \cdot \nabla_{\mathbf{X}} c] = 0, \quad (34)$$

where $\mathbb{D}_0 = D_m \mathbf{C}(\mathbf{X}, t)$ is the effective dispersion tensor, $\mathbf{C}(\mathbf{X}, t)$ is the Cauchy-Green tensor, $\nabla_{\mathbf{X}}$ denotes the gradient with respect to the Lagrangian frame, and the advection term is removed by construction. As the Cauchy-Green tensor at the hyperbolic point \mathbf{x}_h grows as $\mathbf{C}(\mathbf{x}_h, t) \approx \exp[-2\bar{\lambda}(\mathbf{x}_h)t]\hat{\mathbf{s}}\hat{\mathbf{s}} + \exp[2\bar{\lambda}(\mathbf{x}_h)t]\hat{\mathbf{u}}\hat{\mathbf{u}}$, where $\hat{\mathbf{s}}$ and $\hat{\mathbf{u}}$ are the stable and unstable eigenvectors and $\bar{\lambda}(\mathbf{x}_h)$ is the local time-averaged Lyapunov exponent, diffusive transport is exponentially retarded (amplified) in the direction of the stable (unstable) manifolds due to fluid stretching. The local dimensionless Lyapunov exponent is computed to be $\bar{\lambda}(\mathbf{x}_h) = 2.45$, and due to the exponential stretching at the hyperbolic point, at long times the width of a solute blob normal to the unstable manifold converges to the dimensionless Batchelor scale $l_B = 1/\sqrt{\text{Pe}\bar{\lambda}(\mathbf{x}_h)} \approx (6.9 \times 10^{-2}) - (6.9 \times 10^{-3})$, i.e., 7–0.7 % of a correlation length ℓ . Hence even highly diffusive solute blobs do not appreciably cross the unstable manifold, which acts as a surface of minimal flux [31] that controls transport and mixing.

Emptying region. As shown in Fig. 4, there exists an “emptying region” (green) located next to the forcing boundary $x = 0$ where solute particles are advected out of the PFHPM flow domain in one period of the flow. The unstable manifolds emanating from the three hyperbolic points H in \mathcal{D} form the part of the boundary of the emptying region, and direct solute particles toward punctuated “discharge regions” along the boundary of the emptying region (indicated by the absence of an unstable manifold along this boundary). As shown by the purple points in Fig. 4, the discharge regions correspond to regions of intense stretching and folding in the emptying region, where solute particles are strongly mixed as they are advected toward the forcing boundary at $x = 0$. Similarly, the forcing boundary is comprised of a fractal distribution of “inflow” and “outflow” regions (indicated by purple points at $x = 0$ in Fig. 4).

VI. GLOBAL SOLUTE TRANSPORT ACROSS PFHPM

In this section, our focus shifts to the analysis of global solute transport across multiple Lagrangian coherent structures (LCSs), considering how solute blobs evolve during their migration from the interior (right) boundary to the forcing (left) boundary. To understand and quantify the global transport of diffusive solute blobs throughout the entire flow domain, we employ several quantitative measures including spatial and temporal moments and the residence time distribution (RTD).

A. Evolution of spatial moments

For all initial locations (A–D), the solute blobs begin in the regular region and subsequently interact with various LCS types as they are transported toward the forcing boundary. To gain insights into the spreading behaviors of the four solute plumes, we examine spatial moment evolution for different Péclet numbers. This involves consideration of the solute particle probability density function (PDF) $p(x, y, t)$, which is related to the concentration distribution $c(x, y, t) = C(x, y, t)\varphi(x, y, t)$ as

$$p(x, y, t) = \frac{c(x, y, t)}{\int_0^1 \int_0^1 c(x, y, 0) dx dy} = \frac{c(x, y, t)}{m_0}, \quad (35)$$

where m_0 is the initial mass of the solute. This PDF can be constructed from the simulation data by recording the positions of solute tracer particles as a function of space and time, and a continuous representation of this PDF can be generated as required via various smoothing kernels. The centroid $\mathbf{x}_c = (\bar{x}, \bar{y})$ of the solute plume is given by the spatial means

$$\bar{x}(t) = \int_0^1 \int_0^1 x p(x, y, t) dx dy \approx \frac{1}{N_p} \sum_{i=1}^{N_p} x_i(t), \quad (36)$$

$$\bar{y}(t) = \int_0^1 \int_0^1 y p(x, y, t) dx dy \approx \frac{1}{N_p} \sum_{i=1}^{N_p} y_i(t), \quad (37)$$

where $x_i(t)$, $y_i(t)$ are the x and y coordinates of the i th particle, respectively. The spread of the plume is defined in terms of the longitudinal and transverse spatial variances

$$\begin{aligned} \sigma_x^2(t) &= \int_0^1 \int_0^1 [x - \bar{x}(t)]^2 p(x, y, t) dx dy \\ &\approx \frac{1}{N_p} \sum_{i=1}^{N_p} [x_i(t) - \bar{x}(t)]^2, \end{aligned} \quad (38)$$

$$\begin{aligned} \sigma_y^2(t) &= \int_0^1 \int_0^1 [y - \bar{y}(t)]^2 p(x, y, t) dx dy \\ &\approx \frac{1}{N_p} \sum_{i=1}^{N_p} [y_i(t) - \bar{y}(t)]^2. \end{aligned} \quad (39)$$

These moments will be used to quantify evolution of the solute plumes as they interact with different LCSs in the flow domain. Figure 6 shows the centroid distance D_c between the steady (s) and periodic (p) cases, defined as

$$D_c \equiv \|\mathbf{x}_{c,p} - \mathbf{x}_{c,s}\|. \quad (40)$$

This relationship is plotted as a function of the blob centroid x -coordinate \bar{x}_p for the periodic case for all initial locations and Péclet numbers. We terminate calculation of the blob centroid once 1% of particles leave the domain, hence no curves extend to the forcing boundary $x = 0$. Figure 6 shows that the centroid distance remains relatively stable (roughly within 1.5 correlation lengths ℓ) as the blobs are transported through the regular region. However, as the blobs approach and interact with other LCS types (KAM islands, stochastic layers, hyperbolic points, and unstable manifolds), we observe significant growth in the separation between periodic and steady cases. For instance, for initial location D, an explosive increase in the centroid distance occurs when the periodic blob encounters the hyperbolic point and associated unstable manifolds. Similarly, for initial point B, holdup of solute blobs in a KAM island significantly increases centroid distance.

Figures 7 and 8 show that dispersion of the solute plume is strongly influenced by the LCS type in the flow domain. For initial locations A–D, the solute plume dispersions in both the steady and periodic flows are similar in the regular region of the periodic flow, but as solute plumes

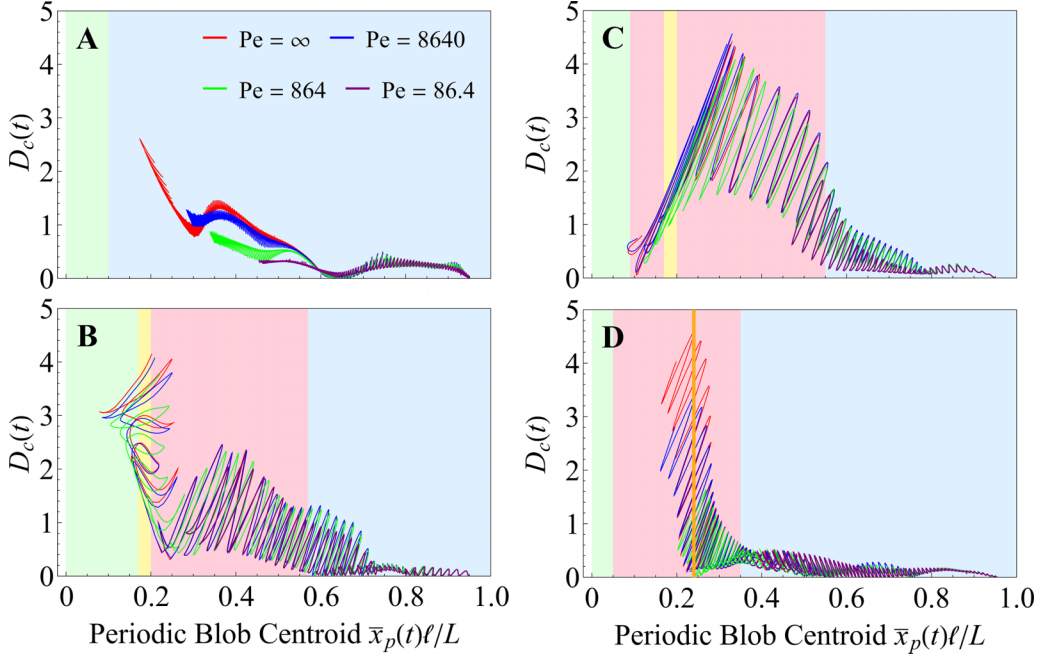


FIG. 6. Centroid distance D_c between solute blobs in the steady and periodic flows as a function of the periodic blob centroid \bar{x}_p for different initial locations [A (top left), B (bottom left), C (top right), and D (bottom right)] and Péclet numbers: ∞ (red), 8640 (blue), 864 (green), and 86.4 (purple). The background colors represent different LCSs in the periodic flow: regular region (light blue), KAM islands (light yellow), stochastic/chaotic regions (light pink), hyperbolic point (orange), and emptying region (light green).

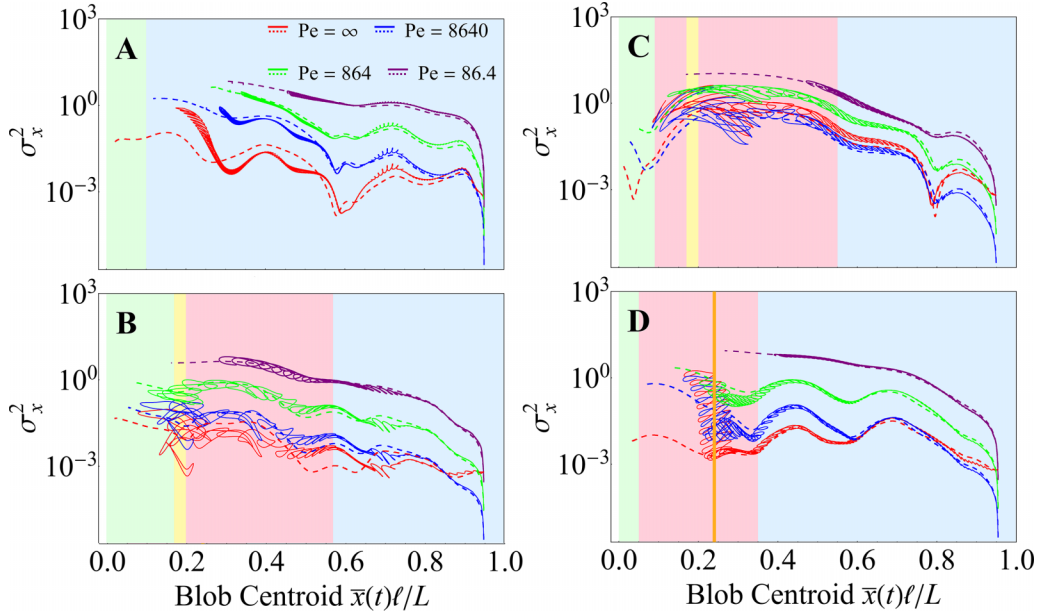


FIG. 7. Plume longitudinal spatial variance σ_x^2 for the steady (dashed line) and periodic (solid line) cases at initial locations A–D, and Péclet numbers ranging from 86.4 to ∞ . Background shading is identical to that of Fig. 6.

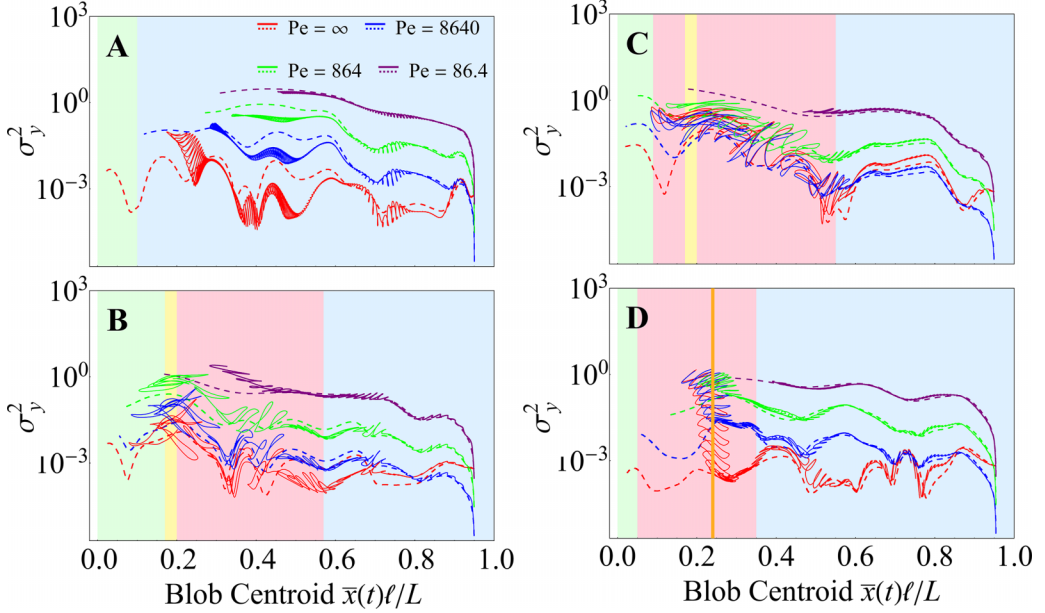


FIG. 8. Plume transverse spatial variance σ_y^2 for the steady (dashed line) and periodic (solid line) cases at initial locations A–D, and Péclet numbers ranging from 86.4 to ∞ . Background shading is identical to Fig. 6.

encounter other LCS types in the PFHPM flow, those with higher Péclet numbers experience strong longitudinal and transverse spreading due to stretching of fluid elements. This is most apparent for initial location D, where interaction of the solute plume for $Pe > 86.4$ with the hyperbolic point and associated unstable manifolds results in growth of both longitudinal and transverse variance several orders of magnitude greater than the corresponding steady flow. Similarly, for initial locations B and C, interaction of the plume with the KAM islands and stochastic layer leads to a significant increase in longitudinal and transverse dispersion beyond that for the steady flow. Conversely, for initial location A, for the periodic case the plume resides mainly in the regular region until exiting near the emptying boundary and so it exhibits similar spreading to the steady case. For all initial locations at a Péclet number of 86.4, dispersion is dominated by diffusive dynamics and so the dispersion is similar for the steady and periodic flows. These results highlight that the LCSs generated by the PFHPM flow can impart unexpected or “anomalous” transport well beyond that generated simply by heterogeneities in the hydraulic conductivity field.

B. Evolution of temporal moments

To quantify the impact of LCSs in PFHPM flow on temporal moments of the solute plume, we consider evolution of the residence time distribution (RTD) $E(\tau)$, which satisfies the unitary condition

$$\int_0^\infty E(\tau) d\tau = 1, \quad (41)$$

where τ is the residence time of solute particles in the PFHPM flow domain. Although the PFHPM is an unsteady flow, for simplicity we only consider solute injection at integer multiples of the forcing period P of the PFHPM, which is much shorter than the mean residence time $\bar{\tau} \gg P$. As such, the RTD is not an explicit function of time t .

Figure 9 illustrates the RTD for the various initial locations and Péclet numbers. For most initial locations and Péclet numbers, the shape of the RTD is broadly similar between the steady and

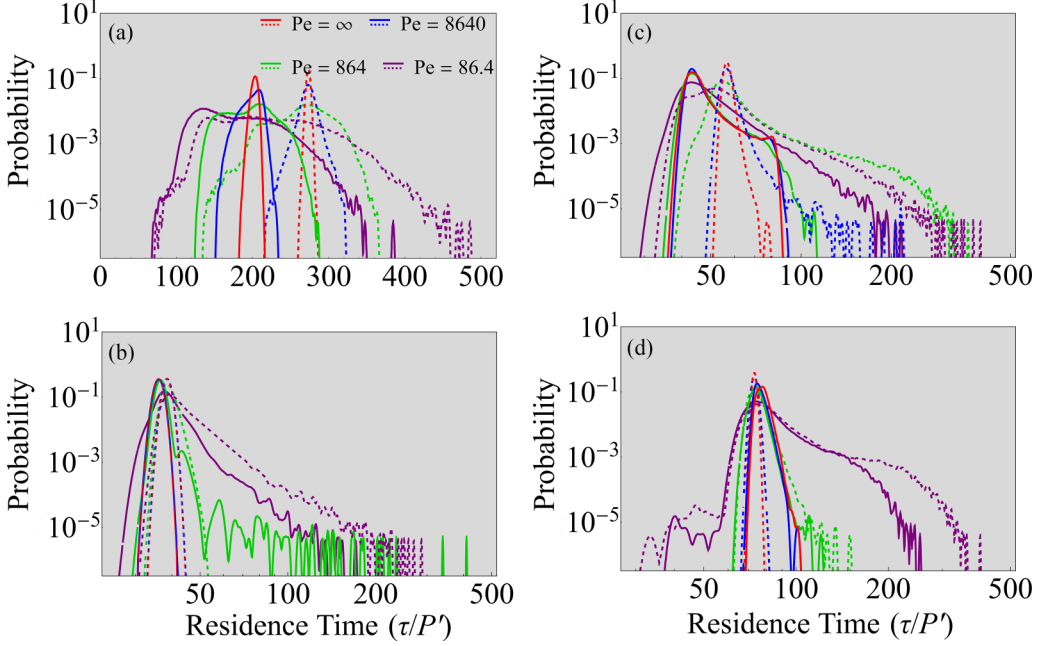


FIG. 9. Residence time distribution (RTD) of solute plumes for the steady (dashed line) and periodic (solid line) cases at four initial locations, with different Péclet numbers.

periodic cases. For initial location A and $Pe > 86.4$, the RTD for the periodic flow is shifted to the left. As solute transport for this initial location is dominated by the regular region, this transport acceleration is attributed to fast transport in the emptying region. For $Pe = 86.4$, diffusion dominates over these effects but a shorter tail is observed in the periodic case due to the emptying region. For initial location B and $Pe > 864$, the RTD for the periodic flow is shifted to the left due to the emptying region. At $Pe = 864$, trapping in the KAM island is significant, leading to the long tail observed for the periodic case. At $Pe = 86.4$, diffusive transport tends to dominate over advective transport, leading to similar RTDs between the steady and periodic cases. For initial location C and $Pe > 86.4$, the RTD in the periodic case is shifted to the left and broadened with a sharp cutoff due to interaction of the solute plume with the stochastic layer. Conversely, for the steady flow for all finite Pe and the periodic case for $Pe = 86.4$, the RTD is observed to have a long tail due to diffusion of particles into low conductivity regions. For initial location D and $Pe > 864$, a longer RTD tail is observed in the periodic case due to hold up of the solute plume at the hyperbolic point and associated unstable manifolds. Conversely, for $Pe \leq 864$, a longer tail is observed for the steady flow due to diffusion into low conductivity regions.

Another measure of interest is the spatially resolved RTD, given by the joint distribution $E_y(\tau, y)$ which quantifies the time and location at which solute particles exit the forcing boundary. $E_y(\tau, y)$ also satisfies the unitary condition and is related to $E(\tau)$ as

$$\int_0^\infty \int_0^1 E_y(\tau, y) dy d\tau = 1, \quad (42)$$

$$E(\tau) = \int_0^1 E_y(\tau, y) dy. \quad (43)$$

Figure 10 shows that for all initial locations and Péclet numbers, solute transport in the steady flow behaves as expected for 2D heterogeneous media, where the solute plumes form well-defined patterns that increase in size with Péclet number. Although some partial splitting of the solute plume

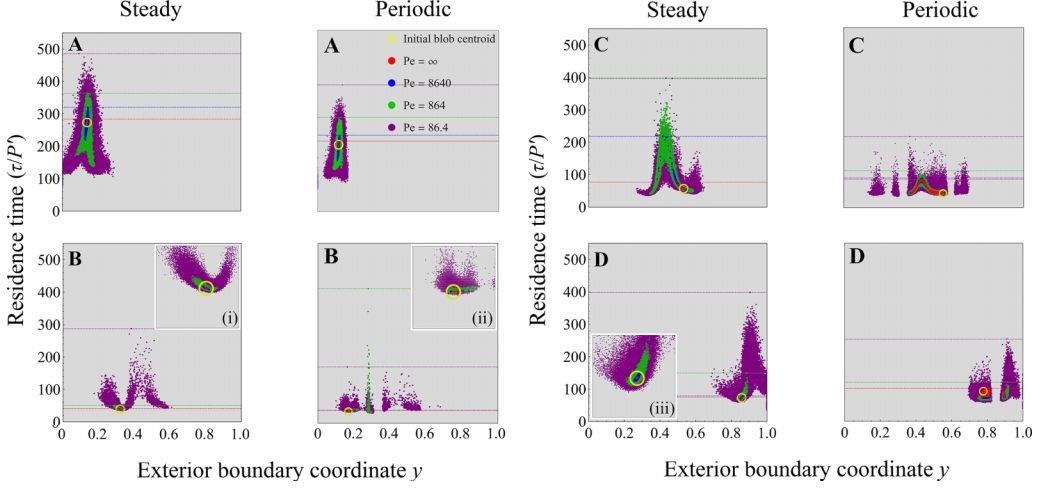


FIG. 10. Spatial residence time distribution (RTD) of solute plumes as they exit the flow domain for the steady and periodic cases at initial locations A–D, with varying Péclet numbers from ∞ (red), 8640 (blue), 864 (green), to 86.4 (purple). The centers of the yellow circles indicate the exit locations of single nondiffusive particles released at the centers of mass of each of the four starting locations. Sample maximum values are indicated by horizontal lines for each Péclet number. The inset figures (i, ii, and iii) offer a magnified view to resolve details within the yellow circle.

is observed for the steady flow due to conductivity inhomogeneities, these events are transient, and in a larger flow domain convergence to an ellipsoidal solute distribution is expected in accordance with dispersion theory. A major topological constraint associated with such steady 2D flows is that streamlines cannot diverge and stagnation points do not occur. These constraints do not apply for the periodic flow, and the various LCS types can impart complex advective dynamics that have a profound impact on solute transport. As such, the solute plume can break up into persistent subplumes due to, e.g., splitting around hyperbolic points as is the case for initial location D. For this initial location and all Pe , the plume is split into two well-defined subplumes that increase in vertical spread and RTD breadth with Pe . For initial positions B and C, the plume interacts with the stochastic regions, stretching and folding the main solute plume before breakup into several distinct subplumes that correspond with the punctuated outflow distributions shown in Fig. 4. Conversely, for initial location A, the solute plume in the periodic flow behaves in a very similar manner to that of the steady flow due to transport through the regular region. For this case, the action of the emptying region does reduce the residence time of the plume slightly.

VII. CONCLUSIONS

When subject to unsteady forcing, saturated heterogeneous poroelastic media such as biological tissue, aquifers, and magma/mantle systems exhibit strong interactions between fluid flow and deformation of the porous matrix that give rise to attenuation of the pressure signal, and to phase lags and transient vorticity. In this study, we show that this coupling also generates complex advective dynamics which markedly alters transport of diffusive species such as solutes, colloids, and chemical and biological species. These complex dynamics arise as a direct result of the interplay between heterogeneous conductivity, medium compressibility, and transient forcing. We consider the specific case of flow and transport in a model periodically forced heterogeneous poroelastic medium (PFHPM) that is driven by a steady pressure gradient across the flow domain coupled with an oscillatory pressure gradient at one boundary.

The complex advective dynamics that result include a rich array of Lagrangian coherent structures (LCSs), topological features (in the Lagrangian frame) that organize advective transport and include localized regions of rapid chaotic advection (stochastic layers), trapping regions (KAM islands), and transport barriers (stable/unstable manifolds) that completely govern mixing and transport of nondiffusive tracers. In the presence of diffusion, we find these kinematic structures also control solute transport and lead to strongly anomalous transport that is fundamentally different from that of, for example, steady flow in heterogeneous poroelastic media or transient flow in homogeneous poroelastic media. Although the details of flow and transport in other unsteady heterogeneous poroelastic systems will differ from that of the PFHPM flow, the basic solute transport characteristics and LCS types are expected to arise in other unsteady saturated poroelastic systems.

We find that the spatial distribution (Lagrangian topology) of these LCSs in the PFHPM is highly heterogeneous, and this has a significant impact upon the transport of diffusive solutes, especially with respect to initial positions of solute plumes. For example, for some initial locations, solute plumes can travel through the “regular” LCS region of the flow domain, which is characterized by transport similar to that of the corresponding steady flow. Conversely, other initial locations lead to interactions with different LCS types such as KAM islands or stochastic regions, leading to strongly anomalous transport, such as trapping of solutes, accelerated mixing, and segregated transport that cannot occur in steady heterogeneous Darcy flow.

LCS types such as KAM islands form transport barriers that are impervious to nondiffusive species but represent regions of slow transport for diffusive species, which effectively “trap” species for a long amount of time before releasing them on a similar time scale. This transport mechanism is similar to that of a very low conductivity region in a strongly heterogeneous porous medium. Conversely, other LCS types such as 1D unstable manifolds exponentially retard (accelerate) diffusive transport normal (parallel) to these manifolds, so that even highly diffusive species do not cross these transport barriers. These unstable manifolds form part of the boundary to the “emptying region” of the flow domain (defined as the region of the flow domain where particles leave within one forcing period), while the remainder of the boundary is comprised of punctuated “discharge regions” where solutes are rapidly transported through the emptying region and out of the flow domain. As such, these unstable manifolds rapidly transport diffusive solutes along the boundary of the emptying region to discharge regions where they are ejected. Rapid solute transport is observed in stochastic LCSs that exhibit chaotic advection, where exponential stretching and folding of fluid elements leads to accelerated transport in the high Péclet number regime.

Collectively, these LCSs generate highly anomalous solute dispersion characteristics, some of which persist at low Péclet numbers, and involve phenomena such as altered spatial and temporal moments of the solute plume and breakup of the plume into persistent subplumes. Such anomalies go beyond those observed for steady flow in strongly heterogeneous porous media, and can only be understood by resolving the LCSs of these complex flows. In general, the interplay of poroelasticity, medium heterogeneity, and unsteady forcing has a profound and unexpected impact upon the dispersion of diffusive solutes that has significant implications for applications that span biological, geophysical, and engineering applications.

APPENDIX A: VELOCITY CORRECTION

Using the mass conservation constraint (7) and expanding the derivative terms, the dimensional advection-diffusion equation (ADE) (15) becomes

$$\varphi \frac{\partial c}{\partial t} + [\mathbf{q} - D_m \nabla \varphi] \cdot \nabla c - D_m \varphi \nabla^2 c = 0. \quad (\text{A1})$$

Dividing through by φ , this becomes

$$\frac{\partial c}{\partial t} + \left[\frac{\mathbf{q}}{\varphi} - D_m \nabla (\ln \varphi) \right] \cdot \nabla c - D_m \nabla^2 c = 0. \quad (\text{A2})$$

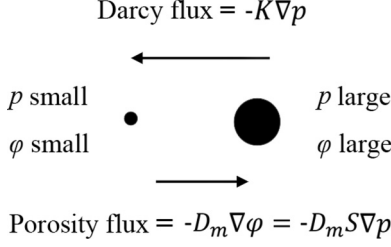


FIG. 11. Darcy flux goes from high pressure to low pressure, but due to porosity gradients a countering squeeze flux develops from lowered porosity in the low-pressure region. Circles are meant to suggest relative pore size.

This equation conveniently places all reference to porosity into the bracketed term. Moreover, as the term in brackets is the velocity $\mathbf{v} = \mathbf{q}/\varphi$ modified by the gradient of porosity, we can define a modified velocity as

$$\mathbf{v}^* = \mathbf{v} - D \nabla (\ln \varphi). \quad (\text{A3})$$

In our simplest, compressible version of poroelastic flow [6], the porosity is linearly coupled to the pressure via the compressibility S , i.e.,

$$\varphi = \varphi_0 + S p, \quad (\text{A4})$$

where φ_0 is the reference porosity and p is the pressure, with a reference pressure assumed to be already scaled to zero for convenience. We note that the two terms that make up \mathbf{v}^* have similar forms: both vary as $\nabla p/\varphi$ with different coefficients. Therefore, we anticipate being able to combine Eq. (A3) into one term. As $\nabla \varphi = S \nabla p$ (because S is assumed constant throughout the domain), using Darcy's law, Eq. (A3) becomes

$$\begin{aligned} \left[\frac{\mathbf{q}}{\varphi} - D_m \nabla (\ln \varphi) \right] &= \frac{K \nabla p - D_m S \nabla p}{\varphi} \\ &= K \left(1 - \frac{D_m S}{K} \right) \frac{\nabla p}{\varphi}. \end{aligned} \quad (\text{A5})$$

This suggests that the relevant dimensionless group controlling the importance of porosity gradients relative to Darcy flux is

$$\text{Po} = \frac{D_m S}{K}. \quad (\text{A6})$$

Po is the ratio of the direct counterflux driven by porosity gradients to the Darcy flux. When $\text{Po} \ll 1$, the effects of porosity gradients are negligible. Physically, Darcy flux flows from high pressure to low pressure while the low-pressure side has lower porosity squeezing fluid out (see Fig. 11) to generate the porosity flux. The modified \mathbf{v}^* becomes

$$\mathbf{v}^* = (1 - \text{Po}) \mathbf{v}. \quad (\text{A7})$$

Typically, $S \ll 1$ and the solute diffusivity D_m is small, so by Eq. (A6) we obtain $\text{Po} \ll 1$ for many geological and biological systems, and thus $\mathbf{v}^* \approx \mathbf{v}$. Hence we may treat Eq. (15) as the standard advection-diffusion equation

$$\frac{\partial c}{\partial t} + \nabla \cdot (\mathbf{v}c) - D_m \nabla^2 c = 0. \quad (\text{A8})$$

TABLE II. Dimensional parameters for PFHPM flow.

Parameter	Symbol	Value
Domain size	L	1 (m)
Mean conductivity	K_{eff}	2×10^{-4} ($\text{m}^2 \text{Pa}^{-1} \text{s}^{-1}$)
Correlation length	ℓ	0.049 (m)
Reference porosity	φ_{ref}	2×10^{-3} (—)
Compressibility	S	10^{-3} (Pa^{-1})
Mean gradient	J	0.1 (Pa m^{-1})
Forcing amplitude	g_p	1 (Pa)
Forcing period	P	1 (s)
Molecular diffusivity	D_m	$(0 - 5.67) \times 10^{-6}$ ($\text{m}^2 \text{s}^{-1}$)

APPENDIX B: SCALING ANALYSIS

Nondimensionalization of the governing equations in Sec. II differs from that applied in previous studies [6,25,26] as inclusion of solute transport via the ADE (14) in this study imposes additional constraints on the nondimensionalization process. In contrast to previous studies [6,25,26,39], here we do not nondimensionalize length with respect to the domain size L , as the primary focus of this study is the solute transport dynamics local to the forcing boundary (left, $x = 0$) in Fig. 1 for the case in which the location of the fixed pressure boundary (right, $x = L$) in Fig. 1 does not affect these dynamics. As such, the horizontal extent L of the domain is considered to be significantly larger than the length scale l_a associated with attenuation of the oscillatory pressure $g(t)$ imposed at $x = 0$, i.e., $L \gg l_a$. In this regime, L has no bearing on the solute transport dynamics local to the oscillatory boundary, and so it is not a physically relevant parameter. Instead, we choose the correlation length scale ℓ of the conductivity field $K(\mathbf{x})$ as the characteristic length scale, as the heterogeneities in $K(\mathbf{x})$ on this length scale generate vorticity that in turn generates transport complexity in the PFHPM flow. The length scale ℓ then yields a natural pressure scale $J\ell$ given by the mean pressure difference over a correlation length, which leads to the remaining scalings described in Sec. III.

From the dimensional periodic pressure equation (10) with a homogeneous conductivity field $K(\mathbf{x}) = K_{\text{eff}}$, the attenuation length scale $l_a \equiv \sqrt{K_{\text{eff}}/(S\omega)}$ of the pressure fluctuation from the oscillatory boundary decays exponentially as $p_p \sim \exp(-x/l_a)$ (see Fig. 2), where x is a dimensional quantity in this expression. Hence the Townley number \mathcal{T} in the dimensionless periodic pressure equation (18) characterizes the ratio of the attenuation length l_a to the characteristic length scale ℓ as (24). The quantity $L/l_a = \sqrt{\mathcal{T}}L/\ell$ characterizes the number of attenuation length scales that are contained in the domain \mathcal{D} , where $\exp(L/l_a) \gg 1$ is the condition for the fixed pressure boundary to have a negligible impact on solute transport local to the oscillatory boundary at $x = 0$.

Due to the length scale ℓ , the Townley number \mathcal{T} and forcing strength \mathcal{G} used in this study differ from the original values used in [6,25,26]. The current values \mathcal{T} , \mathcal{G} can be mapped from these original values as $\mathcal{T} \mapsto \ell^2/L^2 \mathcal{T}$, $\mathcal{G} \mapsto L/\ell \mathcal{G}$. Although it is not generally desirable to alter the definition of these governing parameters, this is outweighed by the benefit of a consistent set of physically relevant dimensionless parameters.

In contrast to previous studies, the dimensionless forcing period $P' = P/\tau_a$ and the domain size $L' = L/\ell$ are no longer scaled to unity, but under the current scalings the dimensionless correlation length scale is scaled to unity. Hence the full parameter set for solute transport in the PFHPM flow is $(\mathcal{T}, \mathcal{C}, \mathcal{G}, \text{Pe}, P, \sigma_{\ln \kappa}^2)$, and for the SHPM flow the parameter is $(\mathcal{T}, \mathcal{C}, \text{Pe}, \sigma_{\ln \kappa}^2)$ as $\mathcal{G} = 0$ and P is irrelevant for the steady case.

For completeness, Table II provides numerical values for the dimensional parameters that provide a basis for the simulations in this paper. These values correspond to a notional bench-scale porous

medium experiment; other systems may be catered for by varying parameter values according to the context of choice. These values then fix the key dimensionless parameter values as listed in Table I.

APPENDIX C: VERIFICATION OF DIFFUSIVE MAPPING METHOD

In Sec. III B, we introduced the operator splitting method known as the diffusive mapping method (DMM) to add particle diffusion to the advective transport of solute particles as an approximation to the Langevin equation (13). Depending upon the order of the advection and diffusion operations, time-stepping can be achieved via “advection then diffuse” (AD), “diffuse then advect” (DA), or “half-step diffusion” (HD) operating splitting approaches over the time increment δt , which, respectively, are represented as

$$\mathbf{x}_{m+1} = \hat{\Phi}_{\text{mod}(m, N_{\text{step}})}(\mathbf{x}_m) + \sqrt{2\delta t/\text{Pe}} \boldsymbol{\xi}, \quad (\text{C1})$$

$$\mathbf{x}_{m+1} = \hat{\Phi}_{\text{mod}(m, N_{\text{step}})}(\mathbf{x}_m + \sqrt{2\delta t/\text{Pe}} \boldsymbol{\xi}), \quad (\text{C2})$$

and Eq. (30). To verify the DMM, we first perform a direct numerical comparison with a finite-element method (FEM) for solute transport in a lattice gyre flow, and then we perform a comparison with the analytic solution for diffusion in a hyperbolic linear flow field.

1. Verification against solute transport in a lattice gyre flow

Here the convergence of the DMM to concentration fields generated by standard FEM techniques is examined in the context of a two-dimensional lattice of perturbed gyre flows [45,46]. Following Froyland and Padberg [46], we establish the streamfunction $\psi(\mathbf{x}, t)$ for a $p \times q$ lattice of gyres on the unit square as

$$\psi(\mathbf{x}, t) = A \sin(\pi f(2px, t)) \sin(\pi qy), \quad (\text{C3})$$

$$f(x, t) = a(t)x^2 + b(t)x, \quad (\text{C4})$$

$$a(t) = \epsilon \sin(\Omega t), \quad (\text{C5})$$

$$b(t) = 1 - 2\epsilon \sin(\Omega t), \quad (\text{C6})$$

where p is the number of gyre pairs repeated in the x direction, and q is the number of rows stacked in the y direction. Here ϵ is the magnitude of the perturbing oscillation of frequency Ω . The chosen parameter values for the perturbed lattice gyre flow are $(p, q) = (2, 3)$, $\epsilon = 0.25$, $\Omega = 2\pi$, $A = 1$, and the solute diffusivity is $D_m = 8.5 \times 10^{-3}$. The corresponding 2D velocity field $\mathbf{v} = \nabla \times \psi \hat{\mathbf{e}}_z$ is complex in that it contains multiple hyperbolic points, and is time-dependent and thus provides nontrivial solute transport phenomena and so represents a useful numerical test of the DMM. Figure 12(a) shows selected vectors of the lattice-gyre flow and the associated solute concentration field generated from the FEM on a grid of over 2.6×10^4 triangular elements in the unit square. Under this flow, the solute blob experiences strong stretching and folding, the former of which is particularly pronounced at hyperbolic points. Comparison of this smooth FEM concentration distribution with the particle-based counterpart requires a method to establish a continuous concentration field from the solute particle assembly computed from the DMM. This is achieved via kernel density estimation, a statistical technique widely used for density estimation in nonparametric statistics [47]. We use the SmoothKernelDistribution function of MATHEMATICA with a bandwidth value selected to provide minimal smoothing at low particle density.

We assess implementation of the DMM under various operator splitting techniques (AD, DA, HD) by transporting $N_p = 5 \times 10^6$ tracer particles in the lattice-gyre flow. As shown in Fig. 12(b), the relative L_2 norm between the DMM and FEM solutions for the solute concentration field varies with both the operator splitting method and the number $N_{\text{step}} = P/\delta t$ of time steps per

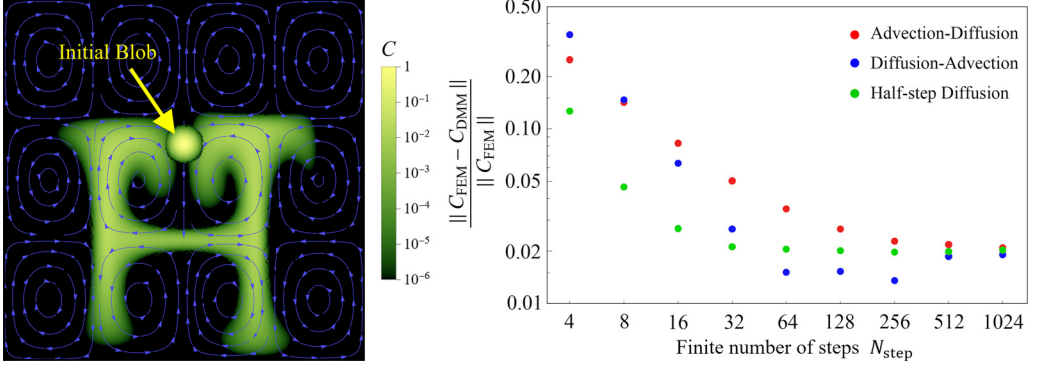


FIG. 12. (a) Lattice gyre FEM solute concentration field C at $t = 0.06$ (green distribution, log scale) for the 2×3 lattice-gyre flow. Also shown are the initial ($t = 0$) flow field (blue vectors) and initial solute Gaussian blob with a 0.1% concentration diameter of 0.055, located at $(x, y) = (0.5, 0.6)$. Asymmetry of the solute concentration field arises from the perturbation strength ϵ . (b) Relative L_2 error between the FEM and DMM methods for the computed solute concentration field in the lattice gyre flow. The L_2 error is reported for different DMM operator splitting methods and temporal resolution.

period. As expected, the AD, DA, and HD splitting methods converge to the same residual error $L_{2,\infty} \approx 0.02$ with increasing N_{step} . The HD splitting method converges to this asymptotic value the fastest due to half-stepping of the diffusion operator, and a value of $N_{\text{step}} = 32$ represents an optimal tradeoff between accuracy and numerical overhead for this scheme. The residual error is attributable to factors originating from both the FEM solution and the DMM method. These factors encompass considerations such as the discretization granularity within the FEM solutions (e.g., the number of elements), the number of discrete particles employed, as well as variations in parameter configurations, including interpolation points and bandwidths, governing the smoothing kernels within the DMM method. It is necessary to acknowledge that, given appropriately optimized particle numbers and smoothing kernel parameters within the DMM method, our approach is demonstrably as accurate as the FEM solution.

2. Verification of DMM for solute diffusion at a hyperbolic point

To verify the DMM against an analytic solution for solute transport, we consider diffusion of a Gaussian solute blob initially placed at the uppermost hyperbolic point H shown in Fig. 4.

As shown in Fig. 13(a), we define a local coordinate system $\mathbf{w} = (w, z)$ relative to the elongated solute blob, where w and z , respectively, are parallel and transverse to the elongated blob. If the origin $(w, z) = (0, 0)$ corresponds to the hyperbolic point H, then the z, w coordinates correspond, respectively, to the stable and unstable manifolds associated with this point. At the hyperbolic point the local velocity field in this coordinate frame is approximated as

$$\mathbf{v}(w, z) \approx \bar{\lambda} w \hat{\mathbf{e}}_w - \bar{\lambda} z \hat{\mathbf{e}}_z, \quad (\text{C7})$$

where $\bar{\lambda}$ is the mean Lyapunov exponent at the hyperbolic point H over one period P of the flow. From (C7), the local deformation gradient tensor $\mathbf{F}(t)$ at the hyperbolic point evolves as

$$\mathbf{F}(t) = e^{\bar{\lambda} t} \hat{\mathbf{e}}_w \hat{\mathbf{e}}_w + e^{-\bar{\lambda} t} \hat{\mathbf{e}}_z \hat{\mathbf{e}}_z. \quad (\text{C8})$$

Following Dentz *et al.* [49], the evolution of the concentration field $c(\mathbf{w}, t)$ of a Gaussian solute blob at the hyperbolic point is

$$c(\mathbf{w}, t) = \frac{m_0}{\sqrt{(2\pi)^2 \det \Sigma(t)}} \exp \left(-\frac{1}{2} \mathbf{w}^\top \cdot \Sigma(t) \cdot \mathbf{w} \right), \quad (\text{C9})$$

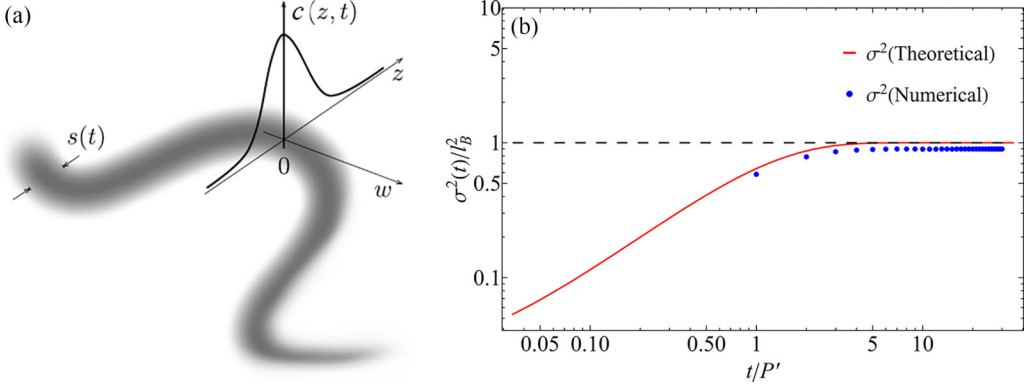


FIG. 13. (a) Schematic of a lamella-shaped scalar concentration field $c(z, t)$ subject to stretching in the w -direction and orthogonal compression in the z -direction. (adapted from Ref. [48]). (b) Evolution of the theoretical (red line) and numerical (blue dots) rescaled transverse blob variance $\sigma^2(t)/l_B^2$ with time toward unity (black dashed line).

where m_0 is the total concentration of the solute blob, and the covariance matrix $\Sigma(t)$ evolves as

$$\Sigma(t) = \mathbf{F}(t) \cdot \left(\Sigma_0 + \frac{2}{\text{Pe}} \int_0^t \mathbf{F}^{-1}(t') \cdot \mathbf{F}^{-\top}(t') dt' \right) \cdot \mathbf{F}^\top(t), \quad (\text{C10})$$

where $\Sigma_0 = \sigma_0^2 \mathbf{I}$ is the covariance matrix of the initial blob. Solution of (C10) yields

$$\Sigma(t) = \sigma_z^2(t) \hat{\mathbf{e}}_z \hat{\mathbf{e}}_z + \sigma_w^2(t) \hat{\mathbf{e}}_w \hat{\mathbf{e}}_w, \quad (\text{C11})$$

where the variances in the z and w directions, respectively, are

$$\sigma_z^2(t) = e^{-2\bar{\lambda}t} \sigma_0^2 + \frac{1}{\bar{\lambda}\text{Pe}} (1 - e^{-2\bar{\lambda}t}), \quad (\text{C12})$$

$$\sigma_w^2(t) = e^{2\bar{\lambda}t} \sigma_0^2 + \frac{1}{\bar{\lambda}\text{Pe}} (e^{2\bar{\lambda}t} - 1). \quad (\text{C13})$$

Hence the blob variance in the w direction grows exponentially, whereas the blob variance in the z direction converges to the Batchelor scale as

$$\lim_{t \rightarrow \infty} \sigma_z^2(t) \rightarrow l_B^2 = \frac{1}{\bar{\lambda}\text{Pe}}. \quad (\text{C14})$$

Equation (C12) can be used to verify the DMM method applied to the uppermost hyperbolic point H in Fig. 4. Here $N_p = 5 \times 10^6$ particles are used to simulate the evolution of a Gaussian solute blob at H with initial covariance $\sigma_0^2 = 1.67 \times 10^{-9}$, and the Péclet number $\text{Pe} = 4.9 \times 10^6$. The local average Lyapunov exponent at H is $\bar{\lambda} = 2.45$. From (C12), the transverse blob variance $\sigma_z^2(t)$ converges toward the dimensionless Batchelor scale $l_B = 2.89 \times 10^{-4}$. As shown in Fig. 13(b), the numerical solution from the DMM closely shadows the theoretical solution, however there exists a very minor difference due to the average Lyapunov exponent approximation $\lambda(\mathbf{x}_h, t) \approx \bar{\lambda}$ used in the theoretical calculation. These results indicate that the DMM is able to accurately resolve convergence of the transverse variance of the Gaussian solute blob to the Batchelor scale.

[1] J. C. Vardakis, L. Guo, T. W. Peach, T. Lassila, M. Mitolo, D. Chou, Z. A. Taylor, S. Varma, A. Venneri, A. F. Frangi, and Y. Ventikos, Fluid-structure interaction for highly complex, statistically defined,

- biological media: Homogenisation and a 3d multi-compartmental poroelastic model for brain biomechanics, *J. Fluids Struct.* **91**, 102641 (2019).
- [2] F. Arega and E. Hayter, Coupled consolidation and contaminant transport model for simulating migration of contaminants through the sediment and a cap, *Appl. Math. Modell.* **32**, 2413 (2008).
- [3] D.-S. Jeng and L. Cui, *Poro-Elastic Theory with Applications to Transport in Porous Media* (CRC, Boca Raton, FL, 2023).
- [4] Y. Zhao and R. I. Borja, A continuum framework for coupled solid deformation-fluid flow through anisotropic elastoplastic porous media, *Comput. Methods Appl. Mech. Eng.* **369**, 113225 (2020).
- [5] T. Sun, S. Ellis, and D. Saffer, Coupled evolution of deformation, pore fluid pressure, and fluid flow in shallow subduction forearcs, *J. Geophys. Res.: Solid Earth* **125**, e2019JB019101 (2020).
- [6] M. G. Trefry, D. R. Lester, G. Metcalfe, and J. Wu, Temporal fluctuations and poroelasticity can generate chaotic advection in natural groundwater systems, *Water Resour. Res.* **55**, 3347 (2019).
- [7] H. Darcy, *Les fontaines publiques de la ville de Dijon. Exposition et application des principes à suivre et des formules à employer dans les questions de distribution d'eau: ouvrage terminé par un appendice relatif aux fournitures d'eau de plusieurs villes au filtrage des eaux et à la fabrication des tuyaux de fonte, de plomb, de toile et de bitume* (Dalmont, 1856).
- [8] M. Fiori, S. Pramanik, and C. W. MacMinn, Flow and deformation due to periodic loading in a soft porous material, *J. Fluid Mech.* **974**, A2 (2023).
- [9] L. Bojarskaite, A. Vallet, D. M. Bjørnstad, K. M. Gullestad Binder, C. Cunen, K. Heuser, M. Kuchta, K.-A. Mardal, and R. Enger, Sleep cycle-dependent vascular dynamics in male mice and the predicted effects on perivascular cerebrospinal fluid flow and solute transport, *Nat. Commun.* **14**, 953 (2023).
- [10] F. Witt, G. N. Duda, C. Bergmann, and A. Petersen, Cyclic mechanical loading enables solute transport and oxygen supply in bone healing: An in vitro investigation, *Tissue Eng., Part A* **20**, 486 (2014).
- [11] R. L. Mauck, C. T. Hung, and G. A. Ateshian, Modeling of neutral solute transport in a dynamically loaded porous permeable gel: Implications for articular cartilage biosynthesis and tissue engineering, *J. Biomech. Eng.* **125**, 602 (2003).
- [12] L. Fan, S. Pei, X. L. Lu, and L. Wang, A multiscale 3d finite element analysis of fluid/solute transport in mechanically loaded bone, *Bone Res.* **4**, 16032 (2016).
- [13] L. Bian, J. V. Fong, E. G. Lima, A. M. Stoker, G. A. Ateshian, J. L. Cook, and C. T. Hung, Dynamic mechanical loading enhances functional properties of tissue-engineered cartilage using mature canine chondrocytes, *Tissue Eng. Part A* **16**, 1781 (2010).
- [14] A. Bonazzi, B. Jha, and F. P. J. de Barros, Transport analysis in deformable porous media through integral transforms, *Int. J. Numer. Anal. Methods Geomech.* **45**, 307 (2021).
- [15] M. S. Cho, F. Solano, N. R. Thomson, M. G. Trefry, D. R. Lester, and G. Metcalfe, Field trials of chaotic advection to enhance reagent delivery, *Ground Water Monit. Rem.* **39**, 23 (2019).
- [16] Y. Wang, D. Fernández-García, G. Sole-Mari, and P. Rodríguez-Escales, Enhanced NAPL removal and mixing with engineered injection and extraction, *Water Resour. Res.* **58**, e2021WR031114 (2022).
- [17] D. H. Kelley and J. H. Thomas, Cerebrospinal fluid flow, *Annu. Rev. Fluid Mech.* **55**, 237 (2023).
- [18] M. Keith Sharp, R. O. Carare, and B. A. Martin, Dispersion in porous media in oscillatory flow between flat plates: Applications to intrathecal, periarterial and paraarterial solute transport in the central nervous system, *Fluids Barriers CNS* **16**, 13 (2019).
- [19] F. Goirand, T. Le Borgne, and S. Lorthois, Network-driven anomalous transport is a fundamental component of brain microvascular dysfunction, *Nat. Commun.* **12**, 7295 (2021).
- [20] R. A. Zimmerman and D. M. Tartakovsky, Solute dispersion in bifurcating networks, *J. Fluid Mech.* **901**, A24 (2020).
- [21] M. K. Rasmussen, H. Mestre, and M. Nedergaard, Fluid transport in the brain, *Physiol. Rev.* **102**, 1025 (2022).
- [22] M. Pool, V. E. A. Post, and C. T. Simmons, Effects of tidal fluctuations on mixing and spreading in coastal aquifers: Homogeneous case, *Water Resour. Res.* **50**, 6910 (2014).
- [23] M. Pool, V. E. A. Post, and C. T. Simmons, Effects of tidal fluctuations and spatial heterogeneity on mixing and spreading in spatially heterogeneous coastal aquifers, *Water Resour. Res.* **51**, 1570 (2015).

- [24] M. Pool and M. Dentz, Effects of heterogeneity, connectivity, and density variations on mixing and chemical reactions under temporally fluctuating flow conditions and the formation of reaction patterns, *Water Resour. Res.* **54**, 186 (2018).
- [25] M. G. Trefry, D. R. Lester, G. Metcalfe, and J. Wu, Lagrangian complexity persists with multimodal flow forcing in compressible porous systems, *Transp. Porous Media* **135**, 555 (2020).
- [26] J. Wu, D. R. Lester, M. G. Trefry, and G. Metcalfe, When do complex transport dynamics arise in natural groundwater systems? *Water Resour. Res.* **56**, e2019WR025982 (2020).
- [27] J. Ottino, *The Kinematics of Mixing: Stretching, Chaos, and Transport* (Cambridge University Press, Cambridge, UK, 1989).
- [28] H. Aref, Stirring by chaotic advection, *J. Fluid Mech.* **143**, 1 (1984).
- [29] G. Metcalfe, D. Lester, and M. Trefry, A primer on the dynamical systems approach to transport in porous media, *Transp. Porous Media* **146**, 55 (2023).
- [30] G. Haller, Lagrangian coherent structures, *Annu. Rev. Fluid Mech.* **47**, 137 (2015).
- [31] R. S. MacKay, Transport in 3d volume-preserving flows, *J. Nonlin. Sci.* **4**, 329 (1994).
- [32] M. Speetjens, G. Metcalfe, and M. Rudman, Lagrangian transport and chaotic advection in three-dimensional laminar flows, *Appl. Mech. Rev.* **73**, 030801 (2021).
- [33] P. K. Kitanidis, The concept of the dilution index, *Water Resour. Res.* **30**, 2011 (1994).
- [34] M. Dentz, J. J. Hidalgo, and D. Lester, Mixing in porous media: Concepts and approaches across scales, *Transp. Porous Media* **146**, 5 (2023).
- [35] J. Bear, *Dynamics of Fluids In Porous Media* (American Elsevier, New York, 1972).
- [36] M. G. Trefry, D. McLaughlin, G. Metcalfe, D. Lester, A. Ord, K. Regenauer-Lieb, and B. E. Hobbs, On oscillating flows in randomly heterogeneous porous media, *Philos. Trans. R. Soc. A* **368**, 197 (2010).
- [37] E. Villermaux, Mixing versus stirring, *Annu. Rev. Fluid Mech.* **51**, 245 (2019).
- [38] C. E. Jacob, Flow of ground water, *Engineering Hydraulics*, edited by H. Rouse (NJ John Wiley, Hoboken, 1950), pp. 321–386.
- [39] L. R. Townley, The response of aquifers to periodic forcing, *Adv. Water Resour.* **18**, 125 (1995).
- [40] L. Li, D. A. Barry, C. Cunningham, F. Stagnitti, and J. Y. Parlange, A two-dimensional analytical solution of groundwater responses to tidal loading in an estuary and ocean, *Adv. Water Resour.* **23**, 825 (2000).
- [41] M. G. Trefry, Periodic forcing in composite aquifers, *Adv. Water Resour.* **22**, 645 (1999).
- [42] M. G. Trefry, D. McLaughlin, D. R. Lester, G. Metcalfe, C. D. Johnston, and A. Ord, Stochastic relationships for periodic responses in randomly heterogeneous aquifers, *Water Resour. Res.* **47**, 2011WR010444 (2011).
- [43] See Supplemental Material at <http://link.aps.org/supplemental/10.1103/PhysRevFluids.9.044501> for figures and animations of advective and diffusive blob evolution in steady and periodic poro-elastic flows.
- [44] J.-L. Thiffeault, Using multiscale norms to quantify mixing and transport, *Nonlinearity* **25**, R1 (2012).
- [45] S. L. Brunton and C. W. Rowley, Fast computation of finite-time lyapunov exponent fields for unsteady flows, *Chaos* **20**, 017503 (2010).
- [46] G. Froyland and K. Padberg, Almost-invariant sets and invariant manifolds – connecting probabilistic and geometric descriptions of coherent structures in flows, *Physica D* **238**, 1507 (2009).
- [47] J. S. Simonoff, *Smoothing Methods in Statistics* (Springer Science and Business Media, Springer New York, NY, 1996).
- [48] E. Villermaux, Mixing by porous media, *C. R. Mec.* **340**, 933 (2012).
- [49] M. Dentz, D. R. Lester, T. Le Borgne, and F. P. J. de Barros, Coupled continuous-time random walks for fluid stretching in two-dimensional heterogeneous media, *Phys. Rev. E* **94**, 061102 (2016).